TISSUE REPAIR

An ILC2-chitinase circuit restores lung homeostasis after epithelial injury

Haerin Jung[1], Do-Hyun Kim[1]†, Roberto Efraín Díaz[2], J. Michael White[3], Summer Rucknagel[3], Lauryn Mosby[1], Yilin Wang[1], Sanjana Reddy[1], Emma S. Winkler[1,4], Ahmed O. Hassan[4], Baoling Ying[4], Michael S. Diamond[1,4,5,6,7], Richard M. Locksley[8,9,10], James S. Fraser[2], Steven J. Van Dyken[1]*

Environmental exposures increase the risk for severe lung disease, but specific drivers of persistent epithelial injury and immune dysfunction remain unclear. Here, we identify a feedback circuit triggered by chitin, a common component of airborne particles, that affects lung health after epithelial injury. In mice, epithelial damage disrupts lung chitinase activity, leading to environmental chitin accumulation, impaired epithelial renewal, and group 2 innate lymphoid cell (ILC2) activation. ILC2s, in turn, restore homeostasis by inducing acidic mammalian chitinase (AMCase) in regenerating epithelial cells and promoting chitin degradation, epithelial differentiation, and inflammatory resolution. Mice lacking AMCase or ILC2s fail to clear chitin and exhibit increased mortality and impaired epithelial regeneration after injury. These effects are ameliorated by chitinase replacement therapy, demonstrating that chitin degradation is crucial for recovery after various forms of lung perturbation. Thus, the ILC2-chitinase response circuit may serve as a target for alleviating persistent postinjury lung epithelial and immune dysfunction.

INTRODUCTION

Lung epithelial cells regulate fluid balance, gas exchange, and the clearance of continuously inhaled airborne particles (e.g., dust, smoke, bacteria, and fungal spores) from the airways. These homeostatic functions are impaired by epithelial cell injury after respiratory viral infection or other lung perturbations. Acute epithelial injury after viral infection is typically followed by a regenerative response that restores homeostasis. However, pathological outcomes, including chronic inflammation, fibrosis, organ failure, and death, can also occur, with morbidity and mortality risk linked to high concentrations of ambient particulate matter (1–5). Although the mechanisms underlying these associations are unclear, a prominent organic constituent of environmental particles is chitin, an insoluble polysaccharide derived from a variety of sources, including dust mites, cockroaches, and molds, that are associated with poor air quality and housing conditions (6–8).

Chitin is present in standard specific pathogen–free animal housing conditions and accumulates in the lungs of acidic mammalian chitinase (AMCase)–deficient mice over time, causing age-related pulmonary fibrosis (9). In the respiratory and gastrointestinal tracts, chitin activates group 2 innate lymphoid cells (ILC2s) via interleukin-25 (IL-25), IL-33, and thymic stromal lymphopoietin (TSLP) to promote lung eosinophil accumulation and alternative macrophage activation (10–13). These hallmarks of type 2 immune activation have also been linked with fibrosis, influenza infection, and severe SARS-CoV (severe acute respiratory syndrome coronavirus)– and SARS-CoV-2–induced lung disease (14–16). However, the environmental drivers of type 2 triggering in such settings are undefined. Environmentally derived chitin accumulates in the airways of humans and mice with age-related pulmonary fibrosis (9) but can be degraded by mammalian chitinases, including AMCase, to lessen inflammatory and fibrotic pathology (7, 9, 17), suggesting that chitin and chitinases shape immune responses and disease persistence after injury. Here, we used mouse models of respiratory viral infection and lung epithelial injury to investigate the contribution of chitin, AMCase, and ILC2s in the restoration of health and epithelial homeostasis after perturbation. Unexpectedly, environmental chitin accumulated in the airways of mice after severe epithelial damage, in disparate settings including influenza A and SARS-CoV-2 infection, bleomycin-induced fibrosis, and after alveolar type 2 (AT2) epithelial cell depletion, concordant with loss of homeostatic AMCase activity. Chitin accumulation altered epithelial regeneration and ILC2 responses after injury, but restoration of chitinase activity was able to counteract these effects, revealing a host-environmental response circuit that contributes to lung homeostasis after epithelial perturbation.

[1]Department of Pathology & Immunology, Washington University School of Medicine, St. Louis, MO, USA. [2]Department of Bioengineering and Therapeutic Sciences, University of California, San Francisco, San Francisco, CA, USA. [3]Department of Pathology & Immunology, Washington University Gnotobiotic Core Facility, Washington University School of Medicine, St. Louis, MO, USA. [4]Department of Medicine, Washington University School of Medicine, St. Louis, MO, USA. [5]Department of Molecular Microbiology, Washington University School of Medicine, St. Louis, MO, USA. [6]Andrew M. and Jane M. Bursky Center for Human Immunology and Immunotherapy Programs, Washington University School of Medicine, St. Louis, MO, USA. [7]Center for Vaccines and Immunity to Microbial Pathogens, Washington University School of Medicine, St. Louis, MO, USA. [8]Department of Microbiology and Immunology, University of California, San Francisco, San Francisco, CA, USA. [9]Department of Medicine, University of California, San Francisco, San Francisco, CA, USA. [10]Howard Hughes Medical Institute, University of California, San Francisco, San Francisco, CA, USA.
*Corresponding author. Email: svandyken@wustl.edu
†Present address: Hanyang Institute of Bioscience and Biotechnology, Research Institute for Convergence of Basic Sciences, Research Institute for Natural Sciences, Department of Life Science, College of Natural Sciences, Hanyang University, Seoul 04763, Republic of Korea.

RESULTS

Injury to AMCase-expressing epithelial cells causes accumulation of environmental chitin

We and others have previously shown that *Chia1* (encoding AMCase) is highly expressed by mature secretory epithelial cells in the lung, particularly club cells and AT2s, consistent with single-cell RNA sequencing (scRNA-seq) data and studies demonstrating that *Chia1*

is induced upon AT2 differentiation (fig. S1, A to C) (9, 18–21). Using a method that enriches for alveolar epithelial cells (22), we compared distal epithelial cells from wild-type (WT) mice with AMCase-reporter [ChiaRed (CR)]–expressing epithelial cells from heterozygous CR mice (9) by scRNA-seq to further verify the cellular identity of AMCase-expressing cells. In the steady state, EpCAM$^+$ cells from WT mice primarily comprised mature AT2 (93%) and *Tm4sf1*-expressing alveolar epithelial progenitor (AEP) cells (~6%) (23, 24). AMCase-expressing CR$^+$ cells matched the transcriptional profile of mature AT2s, as expected on the basis of prior studies (Fig. 1A and fig. S1, D and E) (9, 18, 19). In contrast with AT2s, AEPs were enriched for transcripts marking transitional alveolar epithelial cell states (*Krt8*, *Krt19*, *Cldn4*, and *Cdkn1a*) (fig. S1D), which expand in pathological settings such as severe SARS-CoV-2 infection and pulmonary fibrosis (25–30). In addition, AEPs and AT2s differentially expressed *Epcam*, *Cdh1*, and *H2-Ab1*, encoding cell surface markers EpCAM, E-cadherin, and major histocompatibility complex II (MHC-II), respectively, which were used to distinguish these populations by flow cytometry (figs. S1, D and E, and S2A).

To study the turnover of *Chia1*-expressing cells after epithelial injury, we intranasally inoculated WT and CR mice with influenza A virus (IAV) [A/Puerto Rico/8/1934 (H1N1)], which causes acute epithelial cell loss followed by AEP-mediated alveolar regeneration (24, 31). AT2s and AMCase-expressing (CR$^+$) AT2s were significantly reduced 8 days postinfection (dpi) with IAV. This coincided with diminished AMCase protein in bronchoalveolar lavage (BAL) fluid, followed by recovery of steady-state AT2 numbers and restoration of BAL AMCase by 21 dpi (Fig. 1, B to D). AMCase was exclusively expressed by epithelial cells after IAV infection. CR reporter was not detected in other lung stromal and hematopoietic cells, including macrophage subsets and neutrophils, consistent with prior reports (fig. S2, A and B) (9, 21). The transient loss of AMCase preceded a rapid accumulation of chitin in the lungs of IAV-infected mice (Fig. 1E), suggesting that inhaled particles were abnormally retained in damaged lung tissue niches. Consistent with previous studies (7, 9), we detected chitin in food and bedding materials from two separate animal housing facilities used for these studies (fig. S3, A and B). Thus, this recalcitrant polysaccharide is broadly distributed in standard rodent housing conditions and accumulates in the lungs after epithelial damage.

To further examine the spatial distribution of AMCase-expressing lung epithelial cells, we crossed CR (encoding Cre) with Rosa26-CAG-LSL-zsGreen mice (CR zsG), enabling localization and fate-mapping of AMCase-expressing and zsGreen$^+$ lineage–traced cells (Fig. 1F) (13). In mock-infected mice, AMCase lineage–traced CR zsG$^+$ epithelial cells were uniformly distributed throughout proximal and distal lung regions, reflecting homeostatic AMCase expression in secretory club cells and AT2s (9). However, after injury, AMCase lineage–traced cells were absent in damaged lung areas, with a compensatory increase in the frequency of CR zsG–expressing cells in adjacent uninjured regions (Fig. 1, G and H, and fig. S4A). We verified these expression patterns using antibody staining for AMCase and surfactant protein C (SP-C) as an additional mature AT2 marker, which was coexpressed with the CR zsG reporter in a majority of cells in the steady state and after injury (fig. S4, B to F). These data are consistent with prior reports demonstrating that healthy alveolar epithelial cells are replaced by Krt5-expressing dysplastic epithelial "pods" after severe viral injury (24, 31). Whereas AMCase lineage–traced cells were largely absent from these severely damaged regions early after injury, the frequency of CR zsG$^+$ cells that coexpressed the AEP/transitional epithelial cell marker Krt8 was increased in regions adjacent to damage, where regenerative activity is enriched (Fig. 1, I and J) (24). In addition, rare CR zsG–expressing cell clusters within damaged lung areas increased in size by 21 dpi, consistent with de novo expansion of *Chia1*-expressing cells within regenerating epithelium (fig. S4, G and H). These data suggested that AEP cells induce AMCase during the AT2 recovery phase after epithelial injury, resembling the developmental acquisition of mature AT2 markers during alveologenesis (18, 19, 24). The progenitor:AT2 cell ratio was increased, and CR reporter expression was significantly induced among AEPs at 14 dpi. By contrast, AT2s maintained steady-state CR expression during both the injury and repair phases (fig. S4, I to L). Thus, lung AMCase expression appears to be restored by AEP-driven regeneration after respiratory viral injury.

AMCase is required for restoration of lung health after epithelial injury

The induction of AMCase in AEPs after viral damage suggested that reestablishing chitinase activity may be a key lung tissue adaptation to environmental chitin after severe epithelial injury. To evaluate this hypothesis, we examined IAV responses in AMCase-deficient (CC; ChiaRed) mice, which lack airway chitinase activity (9). Compared with controls, CC mice exhibited increased morbidity and mortality after inoculation with two different doses of IAV [250 and 500 plaque-forming units (PFUs)] (Fig. 2A and fig. S5A). The lower 250-PFU dose was primarily used in subsequent analyses to avoid potential survivor bias. Death among CC mice mostly occurred during the recovery phase after viral clearance, and viral titers were similar between WT and CC mice (fig. S5B), suggesting that differences in disease severity were a result of epithelial injury and environmental chitin accumulation. Chitinase activity was absent (Fig. 2B), and chitin was significantly increased in the BAL fluid of surviving CC mice, compared with controls, for several months after infection (Fig. 2C and fig. S5C). Increased chitin was accompanied by exacerbated lung inflammatory cell infiltration and excessive protein accumulation in the BAL fluid (fig. S5D and Fig. 2D), which contained increased amounts of serum albumin as well as elevated lactate dehydrogenase (LDH) activity (Fig. 2E and fig. S5E), consistent with a sustained loss of barrier integrity (32, 33). Compared with controls, CC mice also exhibited enlarged areas of patchy consolidation by histology (Fig. 2, F to H). In addition, total lung epithelial cells, AT2s, and AEPs were all reduced in CC mice compared with controls (Fig. 2, I to K), indicative of a diminished capacity to restore epithelial barrier function after damage. By contrast, inoculation with low viral doses (e.g., 25 PFU) did not result in mortality, lung epithelial cell loss, or chitin accumulation in WT or CC mice (fig. S5, F to I). Thus, the chitin-chitinase axis was engaged during regenerative responses to severe epithelial injury.

The epithelial defects in IAV-infected CC mice were accompanied by alterations in lung inflammatory infiltrates, which varied in composition at various time points after infection (fig. S6, A to F). Although alveolar macrophages contribute to particle clearance and tissue repair after IAV infection (34, 35), their numbers were similar in the lungs of infected WT and CC mice (fig. S6B). By contrast, γδ T cells and neutrophils were reduced in CC mice as compared with controls (fig. S6, E and F), consistent with enhanced activation of

Fig. 1. Injury to AMCase-expressing cells causes accumulation of environmental chitin. (**A**) Gating scheme and t-distributed stochastic neighbor embedding (tSNE) plots representing scRNA-seq analysis of WT (3334 cells) or CR⁺ (4489 cells) epithelial cells from the lungs of WT or CR-heterozygous reporter mice (K-means clustering of populations comprising >5% of total). (**B** to **J**) Mice were intranasally mock-infected with PBS or inoculated with 250 PFU of IAV and analyzed at the indicated dpi. (B) Total EpCAM⁺MHCII⁺ AT2 cells pooled from each experiment (n = 9 to 20 mice, N = 3 to 5 experiments per time point), (C) CR⁺ lung cells (n = 6 to 14 mice, N = 3 to 5 experiments per time point), (D) AMCase protein in BAL (n = 10 to 20 mice, N = 3 experiments), and (E) chitin in BAL fluid (n = 15 to 24 mice, N > 5 experiments per time point) of IAV or mock-infected WT or CR mice at the indicated time points after infection. R.U., relative units. (F) Mouse breeding scheme to generate AMCase lineage-tracer [CR × R26(LSL)-zsGreen] (CR zsG) mice. (G) Quantification of AMCase lineage–traced zsG⁺ (green) cells in indicated lung areas and (H) representative lung sections from CR zsG mice after IAV or mock infection. Scale bar, 200 μm. Red boxes indicate higher magnification in (I), and the dotted line demarcates injured and uninjured areas. Representative images from n = 3 mice per group, N = 3 experiments. (I) Representative lung sections from CR zsG mice stained with keratin 8 (KRT8, red). Scale bar, 20 μm. Yellow arrowheads, CR zsG⁺KRT8⁺ cells. The yellow box indicates the subsection of the infected lung, with individual channels represented on the right. (J) Quantification of KRT8 costaining within AMCase lineage–traced zsG⁺ (green) cells from IAV (14 to 21 dpi)- or mock-infected mice. Data represent individual biological replicates and are presented as means ± SE. P values were calculated using [(B) to (E)] one-way ANOVA with Dunnett's multiple comparisons test, (G) the Holm-Šidák method, or (J) unpaired t test. *P < 0.05; **P < 0.01; ***P < 0.001; ****P < 0.0001.
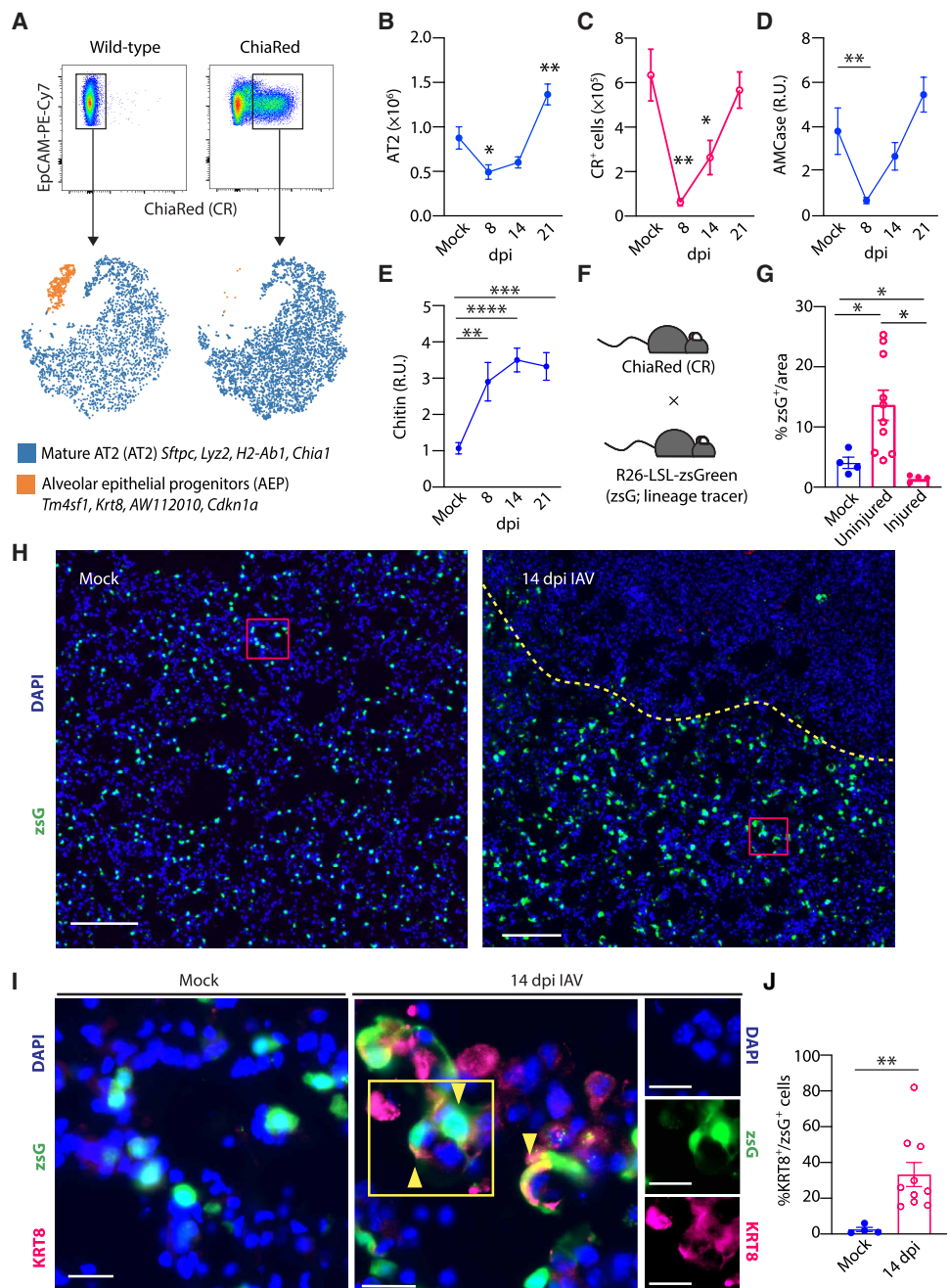
type 2 immune pathways during the repair phase after severe IAV infection. Accordingly, ILC2s and eosinophils, which are induced in the lungs by chitin exposure (10–12) and have been associated with epithelial repair after IAV (36, 37), were increased in the lungs of CC mice compared with those of controls (Fig. 2, L and M). We used mice expressing reporter alleles for ILC2 signature genes arginase-1 (Yarg; $Arg1^{YFP}$), IL-5 (R5; $Il5^{tdTomato}$), or IL-13 (Smart13; $Il13^{hCD4}$) (38) to confirm the expansion of type 2 cytokine–expressing ILC2s during the recovery phase after IAV infection, as previously noted (fig. S7, A to E) (36, 37). Lung ILC2s remained elevated throughout the recovery phase (Fig. 2L). However, IL-13–producing ILC2s and BAL IL-5 were significantly greater in the lungs of CC mice (fig. S7,

F and G). Rare IL-13–producing T helper 2 cells were also detected during the recovery phase, although their numbers were similar in the lungs of WT and CC mice (fig. S7H).

The ILC2-activating cytokine IL-33, as well as amphiregulin (AREG)—an epidermal growth factor receptor (EGFR)–binding growth factor previously implicated in ILC2-mediated lung epithelial restoration after injury (36)—were also elevated in the BAL of CC mice compared with that of controls (fig. S7, I and J). This suggested that IL33- and ILC2-mediated type 2 immune activation was sustained by chitin after viral injury. In uninfected WT mice, the activation of lung ILC2s with exogenous TSLP and IL-33—signals previously implicated in chitin responses (10–13)—markedly increased

Fig. 2. AMCase is required for restoration of lung health after epithelial injury. (**A**) Survival of WT and CC mice inoculated with 500 PFU IAV. (**B** to **G**) WT and CC mice were inoculated with 250 PFU IAV and analyzed at the indicated dpi. (B) Chitinase activity, (C) chitin (21 dpi; $n = 12$ to 17 mice, $N = 3$ experiments), (D) total BAL protein (21 dpi; $n = 6$ to 8 mice, $N = 3$ experiments), and (E) LDH activity (14 dpi; $n = 3$ to 6 mice, $N = 2$ experiments) in BAL from the indicated mice. (F) Representative H&E-stained lung sections at 14 and 21 dpi ($n = 4$ or 5 mice per group) and (G) and (**H**) quantification of inflamed areas at the indicated time points. (**I**) Total lung epithelial cells, (**J**) AT2s, (**K**) AEPs ($n = 3$ to 23 mice, $N \geq 3$ experiments), (**L**) ILC2s, and (**M**) eosinophils ($n = 3$ to 9 mice, $N \geq 3$ experiments) at the indicated time points. (**N**) Dosing regimen of CC mice that received intranasal CHIT1 or hi-CHIT1 after IAV inoculation. (**O**) BAL chitinase activity, (**P**) mean fluorescence intensity (MFI) of CR reporter among CR⁺ epithelial cells, (**Q**) survival, and (**R**) ILC2 numbers in CC mice treated with CHIT1 or hi-CHIT1 21 days after IAV inoculation ($n = 7$ to 9 mice, $N = 3$ experiments). (**S**) Lung ILC2s in WT mice that received intranasal AMCase or hi-AMCase after IAV inoculation [21 dpi; dosing regimen as in (N)]. Dotted lines in (F) indicate inflamed areas, and red boxes indicate insets for higher magnification. Scale bars, 1 mm (top) and 200 μm (bottom). Data represent individual biological replicates and are presented as means ± SE. Survival rates in (A) (WT IAV, $n = 85$ mice; CC IAV, $n = 89$ mice, $N > 5$ experiments) and (Q) (CHIT1, $n = 13$ mice; hi-CHIT1, $n = 10$ mice) were compared by log-rank (Mantel-Cox) test. P values were calculated using two-way ANOVA with multiple comparisons using [(I) to (M)] the Holm-Šidák method. All other P values were calculated by unpaired t test. *$P < 0.05$; **$P < 0.01$; ***$P < 0.001$; ****$P < 0.0001$.
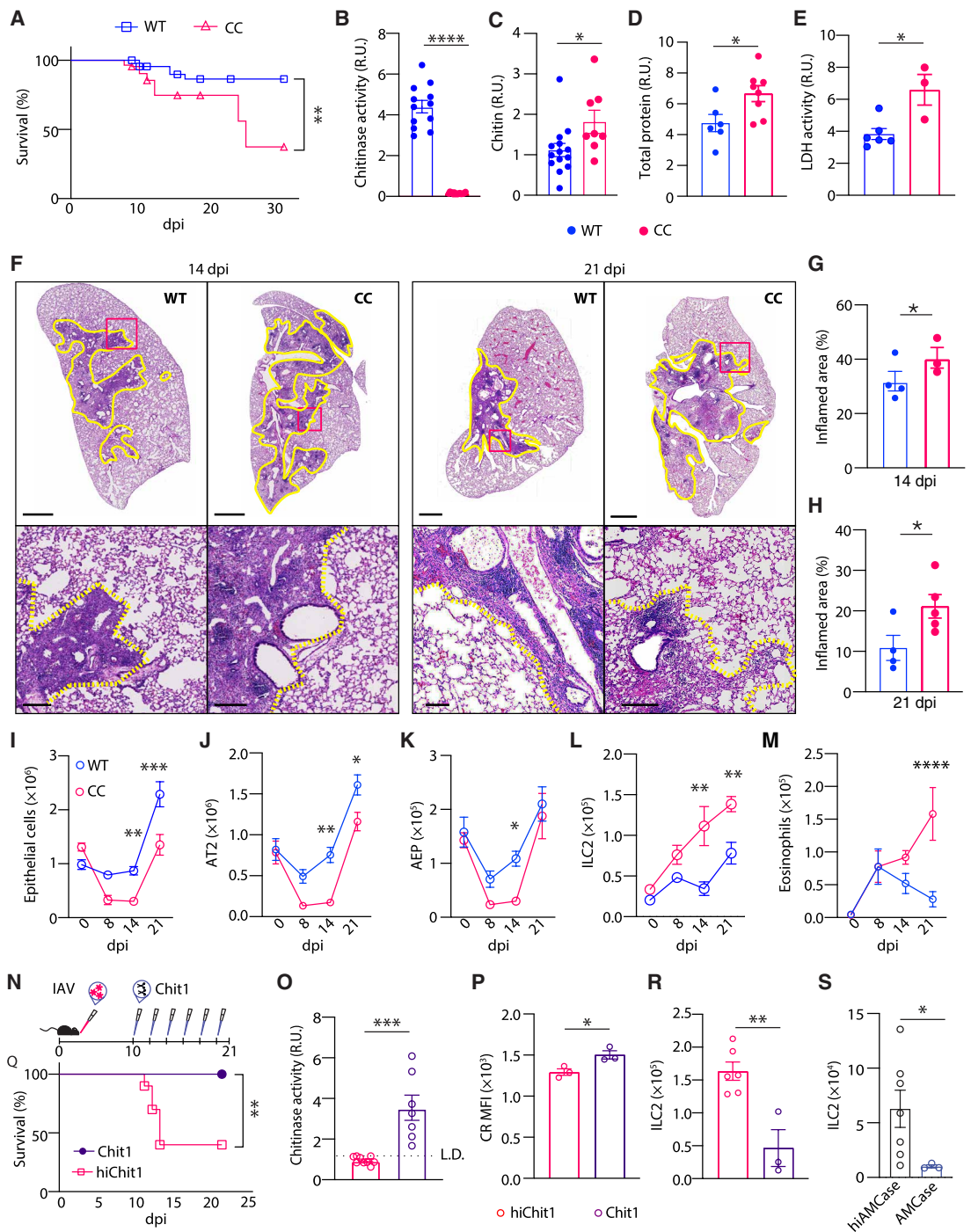
AMCase production and BAL chitinase activity, whereas chitinase activity remained absent in CC mice (fig. S7, K and L). Furthermore, ILC2 activation, IL-13 production, and eosinophil accumulation were significantly enhanced in CC versus WT mice after acute TSLP and IL-33 administration (fig. S7, M to P). Thus, steady-state chitin exposure in the absence of AMCase appears to differentially condition both epithelial and immune compartments in the lungs, preceding severe outcomes after infectious injury and later development of age-related fibrotic lung disease (9).

These results indicated that the inability to restore chitinase activity after infection in CC mice led to increased chitin accumulation, ILC2 activation, dysregulated epithelial repair, and exacerbated lung disease. To test whether exogenous chitinase replacement therapy could rescue these effects, we intranasally administered recombinant chitinases to CC mice during the recovery phase after IAV infection (Fig. 2N). To avoid potential immunogenicity in AMCase-deficient CC mice and to test the sufficiency of chitinase enzymatic activity, we treated with chitotriosidase (CHIT1), another active

mammalian endochitinase similar to AMCase. CHIT1 administration increased BAL chitinase activity and recovery of mature AT2 cells, identified by epithelial AMCase reporter expression (Fig. 2, O and P). Treatment with CHIT1—but not heat-inactivated CHIT1 (hi-CHIT1)—also prevented IAV-induced mortality in CC mice (Fig. 2Q). Administration of either recombinant CHIT1 or AMCase was also sufficient to reduce lung ILC2 expansion in CC and WT mice, respectively, after severe IAV infection (Fig. 2, R and S), suggesting that ILC2s are triggered by environmental chitin after severe epithelial injury. Thus, chitinase enzyme replacement therapy demonstrates efficacy in restoring chitinase activity and aiding recovery after epithelial injury.

To extend these findings to other settings of respiratory virus–induced epithelial injury, we examined chitin and AMCase in mouse models of SARS-CoV-2 infection. Consistent with IAV infection, we observed chitin accumulation in the airways of mice that had been transiently transduced with an adenoviral vector expressing human *ACE2* (AdV-hACE2) (*39*) and inoculated with SARS-CoV-2 (strain WA1/2020) (fig. S8, A and B). At the same time, AMCase expression was lost within the inflamed regions of the lung, demonstrating that SARS-CoV-2 infection also impairs epithelial AMCase in a spatially restricted manner (fig. S8, C and D), akin to IAV infection. AdV-hACE2–transduced CC mice exhibited exacerbated inflammatory lung pathology and prolonged weight loss compared with WT controls after SARS-CoV-2 infection (fig. S8, E to G). Moreover, environmental chitin accumulated in the lungs of mice infected with B.1.351 SARS-CoV-2, a strain naturally adapted to mice. This viral strain also caused more severe lung pathology in CC versus WT mice, whereas viral titers remained similar (fig. S8, H to K). Thus, respiratory viruses appear to cause epithelial damage, which results in the accumulation of environmental chitin. This chitin can then be degraded by AMCase to promote the resolution of inflammation during the post–acute recovery phase.

To circumvent antiviral immune responses and test whether the genetically targeted ablation of AT2 cells was sufficient to trigger chitin accumulation and ILC2 activation, we transiently depleted AT2s using mice expressing an inducible SP-C–driven diphtheria toxin A allele [*Sftpc*tm1(cre/ERT2,rtTA)Hap × *Gt(Rosa)26Sor*tm1(DTA)Lky/J; AT2-deleter] (fig. S9A) (*23*, *40*, *41*). We verified the loss of AT2 cells after tamoxifen administration in AT2-deleter mice (fig. S9B), which exhibited lung edema and increased BAL protein accumulation compared with *Sftpc*cre/ERT2-negative controls (fig. S9, C and D), consistent with AT2 cell deletion and loss of alveolar integrity. AT2 deletion also resulted in reduced BAL AMCase protein and chitinase activity, whereas BAL chitin, lung ILC2s, eosinophils, and AREG were all significantly elevated compared with those in controls (fig. S9, E to K). Other lung-resident immune cells, such as alveolar macrophages, were unaltered by AT2 cell deletion (fig. S9L). Thus, the loss of AT2 cells specifically affects AMCase expression, chitin accumulation, and ILC2 activation.

AMCase prevents severe progressive fibrotic lung disease and mortality
Persistent AT2 cell injury and epithelial regenerative dysfunction are prominent in fibrotic lung diseases (*4*). We therefore tested the involvement of chitin and chitinase in a mouse model of bleomycin-induced pulmonary fibrosis. Bleomycin administration resulted in sustained loss of mature AT2s, accompanied by reduced BAL chitinase activity and accumulation of environmental chitin, which was

significantly increased in the CC mice compared with WT controls (Fig. 3, A to C). CC mice also exhibited increased mortality during the later repair/resolution phase after bleomycin (Fig. 3D), in agreement with the viral infection models and supporting a crucial role for AMCase in promoting the resolution of fibrotic lung disease and survival after injury. By 42 days after bleomycin administration, WT mice had largely resolved fibrosis. However, the lungs from surviving CC mice were marked by prominent interstitial fibrotic lesions (Fig. 3, E and F) and persistently elevated collagen content, which was rescued in CC mice by the expression of a lung-specific AMCase transgene (CC × SPAM Tg mice) (Fig. 3G) (*9*). Moreover, therapeutic administration of recombinant AMCase after bleomycin injury reduced BAL chitin accumulation, improved body weights, and attenuated the severity of lung fibrosis in WT mice (Fig. 3, H to J). Thus, AMCase counteracts the exacerbating effects of environmental chitin in the setting of pulmonary fibrosis, suggesting broad involvement of chitin and AMCase in the repair and regeneration of damaged lung epithelium.

Environmental chitin and chitinase activity control ILC2s and recovery after IAV infection
Our results implicated environmental chitin as a driver of lung disease severity and progression after epithelial injury. We therefore tested whether reducing chitin in the mouse cage environment could affect immune and epithelial recovery after IAV. Because standard mouse housing conditions contain natural sources of chitin (e.g., food and bedding) (fig. S3) (*9*) and are subject to airborne particulate contamination, we reduced environmental chitin by (i) housing mice in sealed positive pressure cages that received double high-efficiency particulate air (HEPA)–filtered air, (ii) using a low dust–generating cellulose-based bedding substrate, and (iii) placing moistened food into feeders located on the cage floor, thereby minimizing inhalation of food dust particles. WT and CC mice were placed in either standard or "low-chitin" caging conditions, acclimated for 1 week, and then intranasally inoculated with IAV (Fig. 4A). Both WT and CC mice housed in chitin-reduced caging conditions maintained body weight (Fig. 4, B and C) and exhibited less airway chitin accumulation (Fig. 4, D and E) and improved epithelial recovery after IAV inoculation compared with mice housed in standard conditions (Fig. 4, F and G). Furthermore, the enhanced lung ILC2 and eosinophil accumulation observed in IAV-infected CC mice housed in standard conditions was ameliorated by reducing environmental chitin (Fig. 4, H and I), implicating chitin as a common environmental driver of type 2 innate immune triggering after respiratory viral infection.

Because AMCase-expressing cells were lost and chitin accumulated in the lungs of IAV-infected WT mice housed in standard conditions, we also tested whether enhancing lung chitinase activity by transgene-mediated overexpression or chitinase therapy could improve epithelial regenerative responses in standard settings. We examined responses to IAV infection in WT mice expressing an SP-C promoter–driven AMCase transgene (SPAM Tg) (*17*). Compared with WT controls, SPAM Tg mice maintained higher BAL AMCase expression (Fig. 4, J and K) and chitinase activity during the recovery phase post–IAV infection (Fig. 4L), concordant with reduced BAL chitin accumulation (Fig. 4M) and improved weight gain during the epithelial recovery phase (Fig. 4N). Transgenic AMCase expression also improved survival (Fig. 4O) and lung epithelial function during the recovery phase after injury because SPAM Tg mice displayed
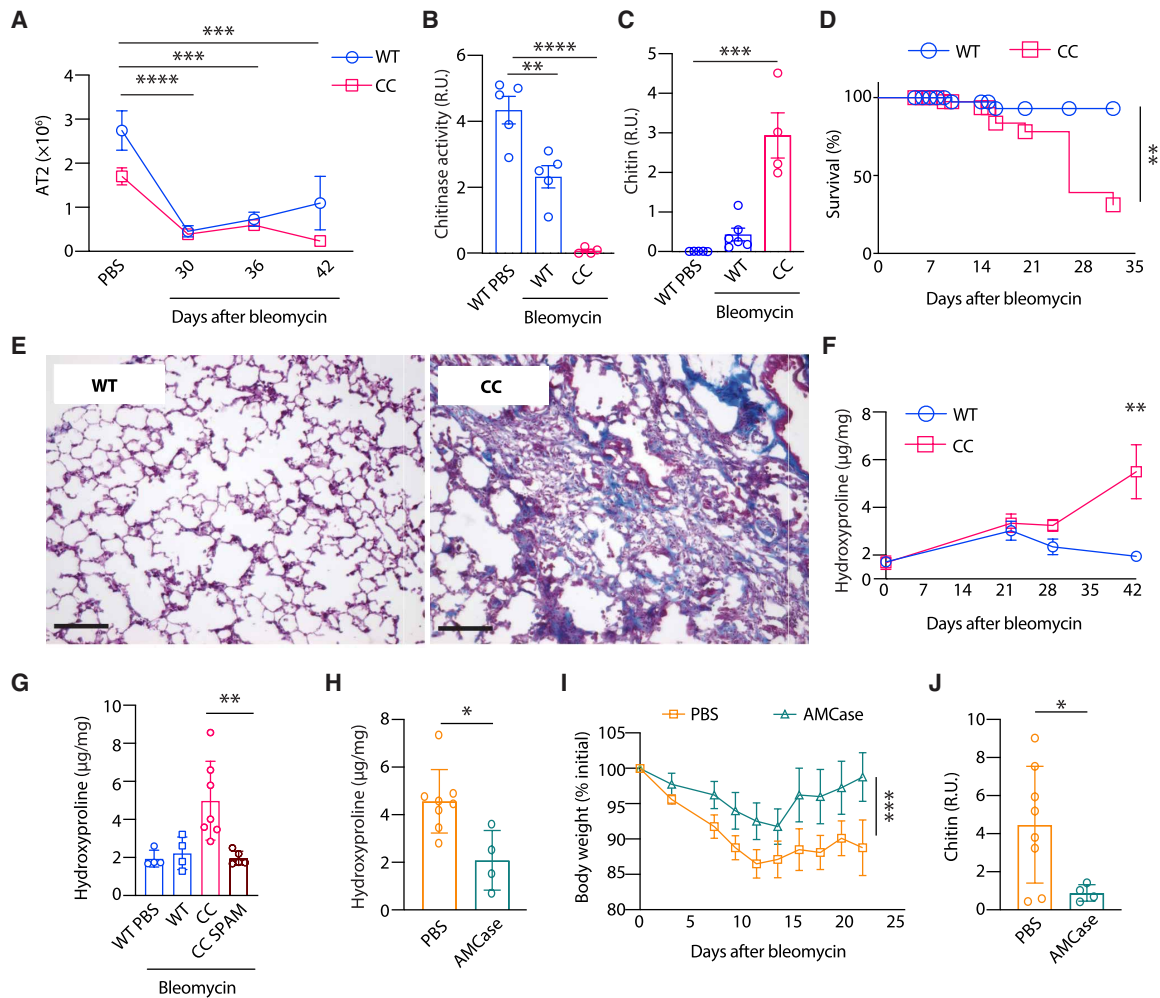
Fig. 3. AMCase prevents severe progressive fibrotic lung disease and mortality. (**A**) Total lung AT2s (n = 4 to 7 mice, N = 3 to 5 experiments per time point), (**B**) BAL chitinase activity, (**C**) BAL chitin (n = 4 to 6 mice, N > 2 experiments), and (**D**) survival of WT and CC mice 21 days after bleomycin challenge (WT, n = 58 mice; CC, n = 63 mice; N ≥ 3 experiments). (**E**) Representative Masson's trichrome–stained lung sections from WT and CC mice 42 days after bleomycin administration (n > 5 mice per genotype; N > 3 experiments). Scale bar, 20 μm. (**F**) Lung hydroxyproline content in bleomycin-challenged WT and CC mice and (**G**) WT, CC, and CC SPAM mice 42 days after bleomycin administration (n = 4 to 7 mice per genotype, N > 2 experiments). (**H**) Lung hydroxyproline, (**I**) body weights, and (**J**) BAL chitin among 21-day bleomycin-challenged WT mice receiving intranasal PBS or recombinant AMCase. Data represent individual biological replicates. P values were calculated by two-way ANOVA with correction for multiple comparisons using (A) Dunnett's method or (F) the Holm-Šidák method, [(B), (C), and (G)] one-way ANOVA with multiple comparisons using Dunnett's method, [(H) and (J)] unpaired t test, (I) paired t test, and (D) log-rank (Mantel-Cox) test. *P < 0.05; **P < 0.01; ***P < 0.001; ****P < 0.0001.

reduced BAL protein accumulation (Fig. 4P) and increased lung AT2 numbers compared with WT controls (Fig. 4Q). In addition, therapeutic administration of recombinant AMCase to WT mice was sufficient to boost BAL chitinase activity (fig. S10A), reduce chitin accumulation (fig. S10B), and improve AT2 recovery compared with heat-inactivated control AMCase (fig. S10C). Thus, enhancing chitin degradation promotes epithelial regeneration and barrier restoration after injury.

Epithelial regeneration is modulated by chitin and chitinase activity

Epithelial cells initiate immune triggering in response to chitin (11, 12, 42) and engage cellular stress pathways in the homeostatic absence of AMCase (9), suggesting that injury-related chitin accumulation might also influence epithelial regeneration and repair. To assess this, we performed RNA-seq on lung epithelial cells

isolated from CC and WT mice in the steady state and during the recovery phase (14 dpi) after IAV infection. AEPs from WT mice induced several genes (false discovery rate–adjusted P < 0.05) and gene pathways involved in epithelial proliferation and differentiation after infection (Fig. 5A and fig. S11A), consistent with the capacity of AEPs to expand and regenerate mature alveolar cells during the recovery phase post–IAV infection (24). Regenerating WT AEPs also induced expression of mature AT1 and AT2 signature genes. By contrast, however, AEPs from infected CC mice failed to induce epithelial maturation markers and proliferation, and differentiation gene pathways were suppressed compared with those in AEPs from WT controls (Fig. 5, B and C), consistent with reduced epithelial cell numbers in CC mice (Fig. 2, I to K). Thus, epithelial regeneration is impaired in the absence of AMCase by environmental chitin.
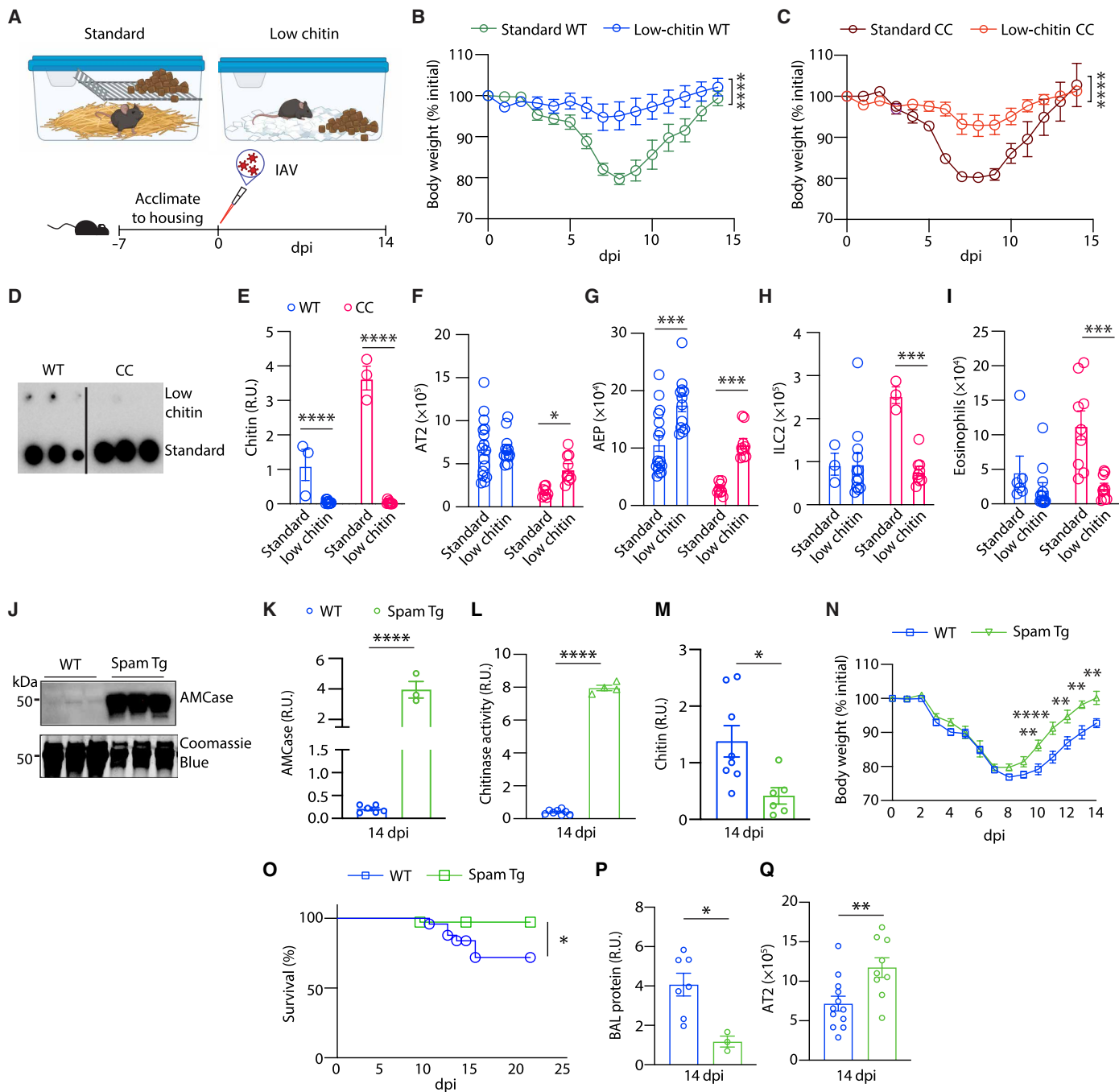
Fig. 4. Environmental chitin and chitinase activity control ILC2 responses and recovery after IAV infection. (**A**) WT and CC mice were acclimated to standard or low-chitin housing conditions before intranasal inoculation with 250 PFU IAV followed by analysis at 14 dpi. (Part of the illustration was created with Biorender.com). (**B**) Body weights of IAV-infected WT or (**C**) CC mice housed in standard or low-chitin conditions. (**D**) Representative chitin blot and (**E**) quantification of BAL chitin, (**F**) total AT2s, (**G**) AEPs, (**H**) lung ILC2s, and (**I**) eosinophils in WT and CC mice housed as indicated (low chitin, $n > 9$ mice per group; standard, $n = 3$ to 15 mice per group). (**J**) Representative image and (**K**) quantification of AMCase (protein immunoblot) and total protein (Coomassie blue stain) in BAL from WT and SPAM Tg mice at 14 dpi ($n = 3$ to 6 mice per group). (**L**) BAL chitinase activity, (**M**) BAL chitin, (**N**) body weights ($n = 3$ to 6 mice per group), (**O**) survival, (**P**) BAL protein, and (**Q**) total AT2s in WT and SPAM Tg mice at 14 dpi. [(K) to (M) and (P)] $n = 4$ to 8 mice, $N = 3$ experiments; (Q) $n = 9$ to 18, three experiments. P values were calculated by unpaired t test [(K) to (M) and (P) and (Q)], two-way ANOVA with multiple comparisons using the Holm-Šidák method [(B) and (C) and (E) to (I)], or (O) log-rank (Mantel-Cox) test (WT IAV, $n = 32$ mice; Spam Tg IAV, $n = 26$ mice, >5 experiments). *$P < 0.05$; **$P < 0.01$; ***$P < 0.001$; ****$P < 0.0001$.
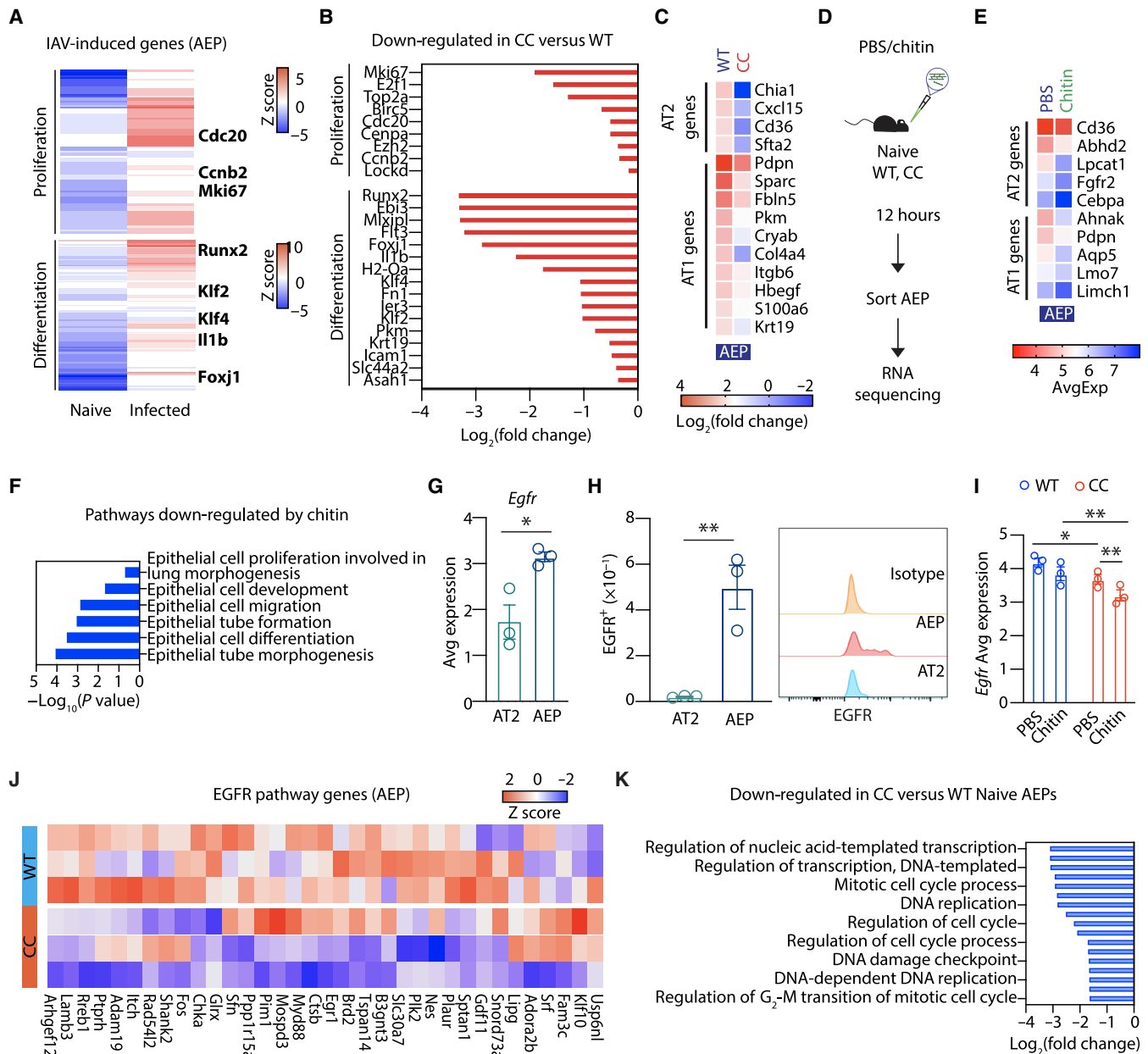
Fig. 5. Epithelial regeneration is modulated by chitin and chitinase activity. (**A**) RNA-seq analysis comparing differentially expressed genes (log$_2$FC $P < 0.05$) in AEPs sorted from the lungs of naïve versus IAV-infected (14 dpi) WT mice and (**B**) down-regulated genes in AEPs from IAV-infected CC versus WT mice. (**C**) Relative expression of AT1 and AT2 marker genes in WT and CC AEPs, shown as log$_2$FC of IAV-infected (14 dpi) as compared with genotype-matched AEPs from naïve mice. (**D**) Experimental approach for AEP sorting after chitin challenge. (**E**) AT1 and AT2 marker gene expression and (**F**) down-regulated GO pathways in AEPs from chitin- versus PBS-treated WT mice. (**G**) Average expression of *Egfr* mRNA and (**H**) EGFR$^+$ AT2s and AEPs in the lungs of naïve WT mice. (**I**) Average expression of *Egfr* in sorted AEPs from WT and CC mice after intranasal PBS or chitin administration. (**J**) EGFR-regulated genes in CC versus WT AEPs after chitin challenge. (**K**) Down-regulated GO pathways in naïve AEPs sorted from the lungs of CC versus WT mice. RNA-seq expression data represent $n \geq 3$ mice per group and were filtered with Benjamini-Hochberg false discovery rate–adjusted P values ≤ 0.05. P values were calculated by unpaired t test (H), *$P < 0.05$; **$P < 0.01$.

To determine whether chitin directly alters epithelial transcriptional programs, we performed RNA-seq analysis on AEPs isolated from the lungs of WT and CC mice 12 hours after intranasal instillation of phosphate-buffered saline (PBS) or chitin (Fig. 5D) (*11*, *12*). In contrast with IAV-induced injury, chitin did not alter lung epithelial cell numbers or the ratio of AEP to AT2 (fig. S11, B to D). However, proliferation and differentiation gene pathways, along with the expression of AT1 and AT2 marker genes, were suppressed in AEPs from chitin-treated mice versus PBS-treated controls (Fig. 5, E and F), indicating that chitin exerts direct effects on regenerative gene expression in AEPs, even in the absence of infectious injury. AEP gene pathways affected by chitin overlapped with proliferation and differentiation programs that were blunted in CC versus WT AEPs after IAV injury (fig. S11E).

Lung epithelial proliferation and differentiation can be promoted by EGFR signaling after injury (*43–45*), and AEPs were relatively enriched in *Egfr* expression compared with AT2s (Fig. 5, G and H), suggesting enhanced responsiveness to the EGFR ligand AREG. Furthermore, *Egfr* mRNA was significantly lower among CC AEPs compared with controls in the steady state and was further diminished by chitin exposure (Fig. 5I). Accordingly, EGFR-regulated genes (*46*) were reduced in CC versus WT AEPs in the steady state and after challenge with chitin (Fig. 5J and fig. S11F), along with alterations in proliferative pathways such as DNA replication and mitotic cell cycle processes (Fig. 5K). Compared with WT, AEPs in CC mice are therefore relatively unresponsive to AREG signaling. This suggests the presence of a negative feedback loop that may prevent uncontrolled proliferation and may account for the failure of AEPs to differentiate in the presence of exacerbated ILC2 responses in CC mice (Fig. 2 and fig. S7). Thus, AMCase plays a role in establishing the lung immune and epithelial set point upon environmental chitin conditioning, which is crucial for healthy recovery after injury.

ILC2s promote epithelial regeneration by restoring AT2 AMCase expression

These data prompted us to further test the involvement of ILC2s on AT2 restoration after injury. Although IL-13 is produced by ILC2s in response to IAV injury, mice lacking IL-4Rα, the common receptor chain for IL-4 and IL-13, showed no differences in morbidity or mortality, chitinase activity, or chitin accumulation (fig. S12, A to D) compared to WT mice after IAV infection. Total epithelial cell recovery and the AEP:AT2 ratio in *Il4ra*$^{-/-}$ mice were also unaltered compared to controls (fig. S11, E to G), indicating that IL-4 and IL-13 signaling is dispensable for chitinase restoration and epithelial recovery after IAV-induced injury. We then further explored the contribution of AREG, which is also produced by ILC2s to influence epithelial recovery after viral injury (*36*). Consistent with this, recombinant AREG administration during the recovery phase induced AEP AMCase expression, increased BAL chitinase activity, reduced chitin accumulation and tissue inflammation, and enhanced AT2 recovery in the lungs of IAV-infected WT mice (Fig. 6, A to H). By contrast, AEP AMCase expression, AT2 maturation, and mouse weight recovery after IAV infection were reduced, and lung inflammation was enhanced by the administration of AREG-blocking antibodies (Fig. 6, I to M). Moreover, administration of the ILC2-activating cytokines TSLP and IL-33 during the recovery phase after IAV significantly increased ILC2 numbers, AREG production, AEP AMCase expression, BAL chitinase activity, and AT2 numbers (Fig. 6, N to R). Thus, the modulation of ILC2s and ILC2-derived AREG appears to influence epithelial regeneration and AMCase restoration after viral injury.

To determine the contribution of ILC2s to the restoration of chitinase activity after epithelial injury, we examined responses to IAV infection in ILC2-deleter [*Il5*$^{tm1.1(icre)Lky}$ × *Gt(Rosa)26Sor*$^{tm1(DTA)Lky}$/J] (*38*) and control R5-Cre [*Il5*$^{tm1.1(icre)Lky}$] mice. We verified that R5-Cre–mediated ILC2 deletion eliminated lung ILC2s before and after IAV infection (fig. S13, A and B). Compared with R5-Cre controls, IAV-infected ILC2-deleter mice exhibited increased morbidity and mortality, particularly during the epithelial recovery phase (Fig. 7A), consistent with prior observations using different ILC2 depletion strategies (*36, 37*) and confirming a crucial role for ILC2s in restoring lung health after viral infection. BAL from surviving ILC2-deleter mice showed elevated chitin amounts and exacerbated

protein accumulation compared with that in controls (Fig. 7B and fig. S13C), along with reduced AREG (fig. S13D), corroborating previous findings demonstrating diminished AREG in ILC2-depleted mice after injury (*36*). The AEP-to-AT2 transition was concomitantly blunted in the lungs of ILC2-deleter mice, along with skewed AEP:AT2 ratios (Fig. 7, C and D). ILC2-deleter mice also exhibited markedly reduced BAL AMCase and chitinase activity compared with control mice, and chitinase activity was additionally reduced in triple knockout (TKO) mice that lack the major ILC2-activating components IL-25, IL-33R, and TSLPR (Fig. 7E and fig. S13E) (*11, 38*). Moreover, AEPs from ILC2-deleter mice failed to induce *Chia1* transcript (Fig. 7F), and total AT2 recovery was significantly diminished in comparison with controls during the recovery phase after infection (Fig. 7G), suggesting that ILC2 deficiency results in an inability to clear chitin due to impaired AT2 maturation and AMCase restoration after injury.

These results suggested that the induction of AMCase crucially mediates the ability of ILC2s to restore epithelial function and lung health after viral injury. In support of this idea, the requirement for ILC2s in AMCase restoration could be bypassed via exogenous administration of AREG (fig. S13F), which was sufficient to restore AEP *Chia1* expression and BAL chitinase activity in IAV-infected ILC2-deleter mice (fig. S13, G and H). Furthermore, active AMCase, compared with a heat-inactivated AMCase control, improved body weight recovery (Fig. 7H) as well as survival among IAV-infected ILC2-deficient mice (Fig. 7, H to J). These improvements were accompanied by increased BAL chitinase activity, reduced BAL chitin and protein accumulation, and significantly improved AT2 cell restoration during the recovery phase in AMCase-treated ILC2-deleter mice compared with controls (Fig. 7, K to N). Thus, chitinase replacement therapy compensates for the loss of ILC2s to promote lung epithelial regeneration after injury, indicating that ILC2s are an essential component of the homeostatic circuit that is engaged to restore chitinase activity after perturbation.

DISCUSSION

Our data demonstrate that a key determinant of lung repair and regeneration after epithelial injury is the ubiquitous environmental polysaccharide chitin, which accumulates in AMCase-depleted lung niches after various forms of epithelial damage. We show that chitin is prevalent in standard, specific pathogen–free mouse housing conditions and influences the severity and persistence of lung disease in commonly used animal models of respiratory viral infection and pulmonary fibrosis. After acute damage, chitin triggers innate immune and epithelial responses that facilitate its own enzymatic digestion by an endogenous glycosyl hydrolase, AMCase. This sequence comprises a host-environmental circuit that drives divergent lung disease outcomes in a chitin- and chitinase-dependent manner. This adaptation to chitin is coordinated by ILC2s, a class of sentinel tissue-resident cells that maintain barrier integrity in several tissues, including lung (*36*), gastrointestinal tract (*13, 43, 47*), and skin (*48*), suggesting that an essential homeostatic function of ILC2s is to impart mucosal barrier cells with specificity for a widespread environmental substrate.

We found that homeostatic chitinase function is compromised by severe respiratory viral infection and fibrotic injury, which affects chitin-mediated inflammatory triggering and epithelial regeneration. Although we show that transient AT2 depletion is sufficient to

Fig. 6. AREG promotes AT2 maturation and chitinase expression after injury. (**A**) Recombinant AREG was administered intranasally to IAV-infected mice every other day from 10 to 21 dpi. (**B**) CR-expressing AEPs and CR MFI after PBS or AREG administration to mock- or IAV-infected (21 dpi) mice (n = 3 to 7 mice per group, N = 3 experiments). (**C**) BAL chitinase activity, (**D**) BAL chitin, (**E**) AT2s, (**F**) AEP:AT2 frequency (as a percentage of total EpCAM⁺ lung epithelial cells; n = 3 to 7 mice per group, N = 3 experiments), (**G**) representative H&E-stained lung sections, and (**H**) quantification of inflamed area in the lungs of IAV-infected mice treated with PBS or AREG at 21 dpi (n = 3 to 5 mice per group, N = 2 experiments). (**I** to **M**) IAV-infected WT mice received intranasal anti-AREG or isotype control antibodies every other day from 10 to 21 dpi. (**I**) MFI of CR-expressing AEPs, (**J**) AT2s, (**K**) mouse body weights, (**L**) representative H&E-stained lung sections, and (**M**) quantification of the inflamed area after anti-AREG or isotype administration (n = 3 to 6 mice per group, N = 3 experiments, 21 dpi). (**N**) Lung ILC2s, (**O**) BAL AREG, (**P**) CR MFI among AEPs, (**Q**) BAL chitinase activity, and (**R**) AT2s in IAV-infected mice that were treated with PBS or IL33 + TSLP between 10 and 16 dpi (n = 5 to 9 mice per group, N = 2 experiments). Bold yellow lines in (G) and (L) indicate inflamed areas. Scale bars, 1 mm. Data represent individual biological replicates and are presented as means ± SE. P values were calculated by (K) paired t test and [(B) and (O)] one-way ANOVA with Šidák's multiple comparison test. All other P values were calculated by unpaired t test. *P < 0.05; **P < 0.01; ***P < 0.001; ****P < 0.0001. ns, not significant.
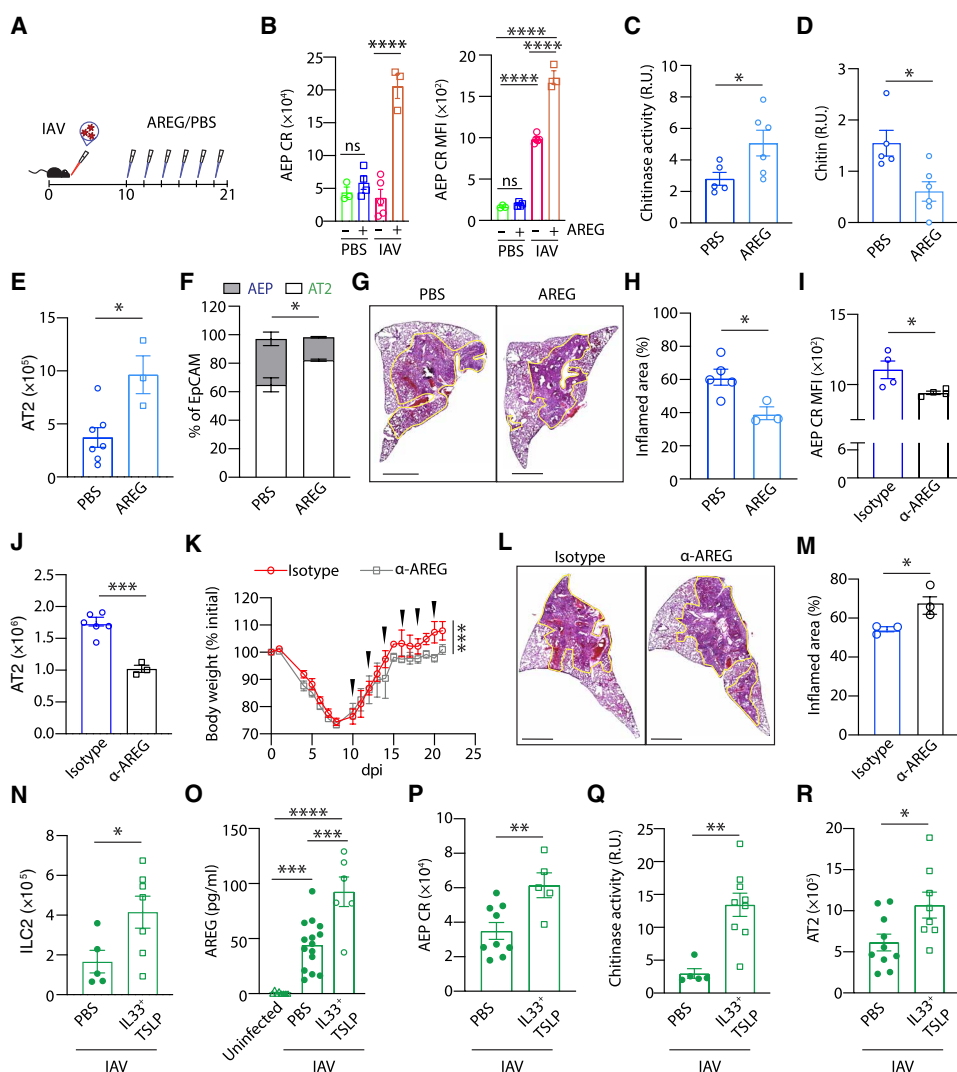
cause loss of AMCase activity and chitin accumulation, other routine particle clearance mechanisms, including mucociliary function and alveolar macrophage phagocytosis, are also impaired in disease settings (*34, 35, 49, 50*), implying that a lack of chitinase and possibly other AT2-derived proteins (e.g., surfactant proteins) is compounded by an overall reduced capacity to maintain the integrity of the airspaces. In humans, high concentrations of airborne particulate matter increase the risk for severe respiratory viral infection, pulmonary disease, and mortality, including COVID-19–related lung epithelial alterations that resemble age-related fibrosis (*1, 2, 5, 28, 29*). Severe COVID-19 lung pathology is marked by cell types and cytokines that are induced by chitin exposure (*10, 11, 14, 16, 17, 30, 51*). In addition, we previously showed that chitin accumulates in the airways of humans with pulmonary fibrosis, as well as in aging mice that genetically lack AMCase (*9*). These findings implicate chitin as a common environmental driver of lung disease severity even among younger, WT mice, induced by both infectious and noninfectious stimuli that cause AT2 cell injury, which impairs critical epithelial-derived chitinase effector function. As we show,

AMCase-deficient mice that are unable to restore chitinase activity exhibit severe lung disease and mortality after AT2 injury.

Our results further identify chitin as an environmental trigger of lung ILC2 activation after respiratory viral infection. Prior studies have established that ILC2s contribute to epithelial repair after IAV (*36*). However, the identity of specific environmental factors that contribute to sustained type 2 immune triggering in postviral lung disease has remained unclear. We show that environmental chitin and lung chitinase activity influence both the lung immune and epithelial cellular landscape in the context of infectious disease, revealing a host-environmental interaction that determines respiratory disease outcomes. After lung epithelial injury, chitin triggers ILC2s to restore homeostasis by inducing AMCase in regenerating epithelial cells, thereby equipping mature AT2s with chitin-degrading capacity required for tissue restoration and resilience. We further demonstrate that this circuit is partially mediated by AREG after IAV. However, this growth factor likely synergizes with a complex network that integrates interstitial macrophages and fibroblasts—among other cellular and growth factor components—to ultimately resolve tissue injury.

Fig. 7. ILC2s control epithelial regeneration by restoring AT2 AMCase expression. (A to F) Mice were intranasally infected with 250 PFU of IAV and analyzed for (A) survival (WT IAV, $n = 13$ mice; ILC2-deleter IAV, $n = 19$ mice), or (B to F) euthanized and analyzed at 14 dpi. (B) BAL protein ($n = 6$ mice per group, $N = 3$ experiments), (C) representative flow cytometry, and (D) frequency of AEP and AT2 cells ($n = 8$ to 15 mice, $N = 3$ experiments). (E) BAL chitinase activity in R5, ILC2-deleter mice and TKO mice after IAV infection ($n = 4$ to 8 mice, $N > 2$ experiments). (F) Quantitative real-time PCR (qPCR) analysis of *Chia1* transcript abundance in AEPs after IAV infection ($n = 3$ to 5 mice per group). (G) Total AT2 cells ($n = 4$ to 6 mice, representative of $N = 3$ experiments) in R5 and ILC2-deleter mice after 21 dpi. (H) Dosing regimen, (I) body weights, (J) survival (ILC2-deleter IAV-AMCase, $n = 22$ mice; ILC2-deleter IAV-hiAMCase, $n = 12$ mice, $N > 3$ experiments), (K) BAL chitinase activity ($n = 4$ to 7 mice, $N = 3$ experiments), (L) BAL chitin ($n = 9$ or 10 mice, $N = 3$ experiments), (M) BAL total protein ($n = 6$ to 8 mice, $N = 3$ experiments), and (N) AT2 numbers ($n = 7$ to 10, $N = 3$ experiments) in ILC2-deleter mice at 21 dpi or as indicated after IAV infection and intranasal administration of active AMCase or hiAMCase. Arrows in (I) and (J) represent active AMCase or hi-AMCase intranasal doses. Data represent individual biological replicates and are presented as means ± SE. *P* values were calculated by [(A) and (J)] log-rank (Mantel-Cox) test, [(B), (D), (F), (G), (I), and (K) to (N)] unpaired *t* test, or (E) one-way ANOVA with the Holm-Šidák method. *$P < 0.05$; **$P < 0.01$; ***$P < 0.001$.
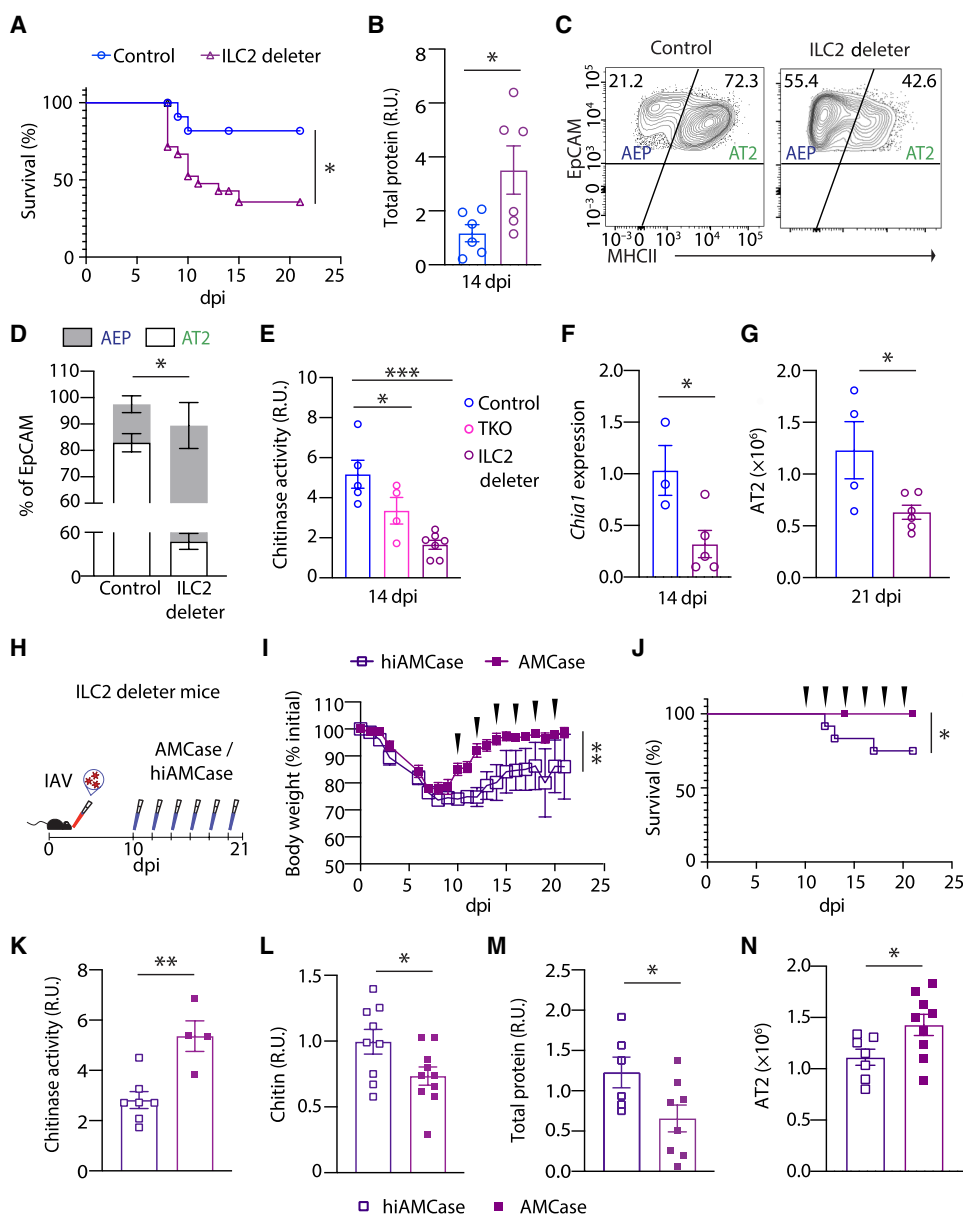
The lack of AMCase led to the development of a nonresolving, progressive lung fibrosis after bleomycin-induced injury, suggesting that chitin accumulation overrides normal mechanisms of epithelial restitution in disparate contexts. Both AEP and ILC2 compartments are consequently altered in the absence of AMCase, both in the steady state and after IAV infection, consistent with low-level homeostatic "conditioning" of ILC2s and AEPs by environmental chitin that subsequently accumulates and impairs recovery after injury. Accordingly, although lung ILC2s from CC mice exhibit increased responsiveness and AREG production in response to stimuli, these signals are coupled with AEPs that express diminished EGFR and associated growth factor components and are therefore relatively unresponsive to differentiation signals because of the suppressive effects of environmental chitin. This conditioning perhaps reflects a negative feedback loop that prevents uncontrolled AEP proliferation in the presence of exacerbated ILC2 responses. Nevertheless, in

the absence of AMCase in the setting of epithelial injury, chitin provokes chronic ILC2 triggering and impairment of epithelial regeneration, resembling epithelial alterations that occur in chronic lung disease, pulmonary fibrosis, rhinosinusitis, and ILC2–stem cell interactions during hair follicle cycling (*4*, *24*, *52*, *53*). Our results suggest that this ILC2-AMCase circuit is broadly involved in shaping responses to epithelial dysfunction and inflammation. Furthermore, it may represent a general feature of insoluble particle–driven stromal alterations and recurrent injury, which may ultimately produce long-lasting alterations in lung architecture and function.

Both ILC2 triggering and lung epithelial impairments can be ameliorated by reducing environmental chitin or by boosting airway chitinase activity, implicating the ILC2-chitinase circuit as a critical determinant of lung health after injury. In addition, we demonstrate that the requirement for ILC2s in restoring epithelial health after IAV infection can be bypassed by exogenous chitinase therapy,

showing that a primary function of ILC2s in mucosal barrier restoration is to coordinate chitinase responses to chitin, analogous to their essential role in driving dietary chitin adaptations in the gastrointestinal tract (13). In humans, *CHIA* gene variants encoding AMCase enzyme isoforms with increased chitinase activity show protective associations among asthma cohorts (54, 55), suggesting that robust enzymatic activity is crucial to degrading chitin-containing stimuli that contribute to chronic airway disease. Here, we show that both active mammalian endochitinases, AMCase and CHIT1, exhibit efficacy in therapeutic targeting of environmental chitin after lung epithelial injury. AMCase and CHIT1 differ with regard to expression patterns, substrate preferences, and pH-dependent activities (56–58), suggesting that engineered enzyme variants might be tailored to improve degradation of naturally occurring substrates in a tissue-specific manner. In conclusion, this work demonstrates that boosting chitinase activity to reduce airway chitin improves lung health after injury, suggesting additional therapeutic avenues for restoring barrier integrity in a wide range of diseases involving epithelial damage.

MATERIALS AND METHODS

Mice

For all experiments, age- and sex-matched mice on C57BL/6J backgrounds were used between 6 and 12 weeks of age and maintained under specific pathogen–free conditions. CR knockin/knockout reporter (CR; *Chia1*^{ChiaRed}) mice (9) were bred with Rosa26-flox-stop-zsGreen [*Gt(Rosa)26Sor*$^{tm6(CAG-ZsGreen1)Hze}$/J; 007906; the Jackson Laboratory] mice to generate AMCase-zsGreen (CR-zsG) reporter/lineage tracer mice and additionally crossed with Smart13 (*Il13*^{hCD4}) (59) reporter mice as indicated. WT SPAM Tg, CC SPAM Tg, TKO (IL-25$^{-/-}$, IL-33R$^{-/-}$, and TSLPR$^{-/-}$), Red5 (*Il5*^{Red5}), Yarg (*Arg1*^{Yarg}), and ILC2-deleter [*Il5*^{Red5} × *Gt(Rosa)26Sor*$^{tm1(DTA)Lky}$/J] mice were bred and maintained as previously described (9, 11, 38). *Sftpc*$^{tm1(cre/ERT2,rtTA)Hap}$ mice, provided by H. Chapman (UCSF), were bred with *Gt(Rosa)26Sor*$^{tm1(DTA)Lky}$/J (009669; Jackson) mice to generate AT2-deleter mice. Whole-body *Il4ra*$^{-/-}$ mice were generated by crossing CMV-cre (006054; the Jackson Laboratory) with *Il4ra*$^{fl/fl}$ mice (60), provided by F. Brombacher (University of Cape Town). All procedures were approved by the Washington University School of Medicine in St. Louis Institutional Animal Care and Use Committee (Assurance #D16-00245).

In vivo treatments

Mice were anesthetized with isoflurane and intranasally inoculated with IAV [A/Puerto Rico/8/1934(H1N1)], which was provided by A. Boon (Washington University School of Medicine), or mock-infected with PBS (30 μl). Transient transduction of mice with AdV-hACE2 and inoculation with 10^5 focus-forming units (FFU) of SARS-CoV-2 strain 2019 n-CoV/USA_WA1/2020 was performed as described (39). Where indicated, the mice were intranasally inoculated with 10^6 FFU of SARS-CoV-2 WA1/2020 D614G, B.1.351 in 50 μl of PBS as described (61). IAV titers were determined by plaque assay on Madin-Darby canine kidney cells. After all challenges, the mice were monitored and weighed daily and humanely euthanized if 30% loss of initial weight occurred. Recombinant mouse AMCase [generated as previously described in (62)], CHIT1 (R&D Systems), or matched control aliquots that were heat-inactivated (5 min, 95°C) were intranasally administered at a dose of 2 μg in 50 μl of PBS every 2 days between 10 and 21 dpi after IAV inoculation.

Recombinant mouse TSLP (10 ng) and IL-33 (500 ng; R&D Systems) were administered intranasally to mice in 50 μl of PBS for 3 consecutive days before euthanasia and tissue collection. Recombinant mouse AREG (5 μg) (R&D Systems), anti-AREG (2 μg) (R&D Systems), and immunoglobulin G (IgG) isotype control (2 μg) (R&D Systems) were administered intranasally to mice in 50 μl of PBS for every 2 days between 10 and 21 dpi after IAV inoculation before euthanasia and tissue collection. Bleomycin (2 mg per kilogram of body weight) (Cayman) was resuspended in PBS and administered to mice intranasally once at the start of the experiment before euthanasia and tissue collection. Tamoxifen (2 μg) (Sigma-Aldrich) was resuspended in 1 ml of peanut oil and administered to the mice intraperitoneally twice a week, every 3 days before euthanasia and tissue collection. Serum was collected from supernatants of non-heparinized blood that was allowed to clot at room temperature for 1 hour. For BAL, sterile PBS (1 ml) was intratracheally instilled and centrifuged for 10 min at 3000*g* before collection of supernatants for biochemical assays. BAL pellets (BALp) were boiled for 5 min to lyse cellular material and denature proteins before assaying for chitin content as described (9).

Standard and reduced chitin housing conditions

For standard conditions, the mice were housed in filter-top cages receiving room air 1 week before placement in negative pressure cages that received double HEPA–filtered air (PNC IVC rack system; Allentown) for IAV infections. Standard cages contained autoclaved corn cob bedding (Andersons) with irradiated PicoLab 5053 Rodent Diet (LabDiet) placed in hoppers located at the top of the cage (as shown in Fig. 2). For low-chitin conditions, the mice were housed in sealed positive pressure cages that received double HEPA–filtered air (Sentry SPP rack system; Allentown) and lined with ALPHA-dri PLUS bedding (Shepherd Specialty Papers), a low dust–generating bedding substrate composed of virgin paper pulp cellulose squares. In addition, PicoLab 5053 Rodent Diet (identical to that used in standard conditions) was moistened and placed into feeders located on the floor of the cage to minimize the inhalation of food dust particles generated during feeding.

Tissue preparation and flow cytometry

The mice were euthanized, and lung immune cells were enumerated by flow cytometry as described (11). Lung epithelial cells were prepared as described (9), with minor modifications. Briefly, the lungs were perfused with 10 ml of PBS through the right ventricle of the heart before intratracheal instillation of 2 ml of dispase II (5 mg/ml) (Thermo Fisher Scientific) and 1 ml of 0.1% low-melting point agarose, followed by cooling with ice in situ for 1 min. Lung lobes were then dissected and incubated in 2 ml of dispase II (5 mg/ml) (Thermo Fisher Scientific) for 45 min at room temperature, transferred to C tubes (Miltenyi) containing 5 ml of deoxyribonuclease I (50 μg/ml) (Sigma-Aldrich), and dispersed into single-cell suspensions using a gentleMACS automated tissue dissociator (Miltenyi). The cells were passed through 100-μm nylon filters, washed, incubated with red blood cell lysis buffer (BioLegend), and resuspended in PBS with 2% fetal bovine serum before Fc blocking with anti-mouse CD16/CD32 (BioXCell) and cell staining.

After Fc blocking, the cells were stained using the antibodies listed in table S1. Live cells were identified via exclusion of DAPI (4′,6-diamidine-2-phenylindole dihydrochloride) (Roche) and enumerated with Precision Count Beads (BioLegend). Flow cytometry

data acquisition and analysis was performed with a BD FACSymphony A3 flow cytometer and FlowJo software (BD Biosciences), and the cells were sorted using a MoFlo XDP (Beckman Coulter).

Biochemical and protein assays

Chitinase activity was measured in BAL supernatants using 4-methylumbelliferyl-N,N'-diacetyl-β-D-chitobioside (Sigma-Aldrich) substrate as described (9) for 30 min at 37°C. Chitin was quantified by dot-blot assay as described (9), with minor modifications. Briefly, 1 μl of BALp and sonicated chitin (Sigma-Aldrich) controls were pipetted onto 0.2-μm nitrocellulose membranes, dried overnight, rinsed in tris-buffered saline containing 0.05% Tween 20 (TBST), blocked for 30 min with 5% bovine serum albumin (BSA) in TBST, and incubated with an enhanced green fluorescent protein (GFP)–labeled chitin-binding probe (48) in 1% BSA/TBST overnight at 4°C with gentle agitation. After washing with TBST, the membranes were incubated with biotinylated anti-GFP antibody (13-6498-82), followed by streptavidin–horseradish peroxidase (HRP) (RABHRP-3) (Invitrogen) (table S1) for 45 min at room temperature, washed, and developed with enhanced chemiluminescence substrate (170-5060; BioLegend) before image acquisition on a ChemiDoc MP (Bio-Rad). For protein and AMCase quantification, equal volumes of BAL supernatant were diluted in 4× Laemmli SDSS–polyacrylamide gel electrophoresis buffer containing 2-mercaptoethanol (Bio-Rad) and incubated at 95°C for 5 min. Samples were then electrophoresed on 4 to 15% TGX protein gels (Bio-Rad), transferred to 0.2-μm nitrocellulose membranes, blocked with 5% milk, and probed with anti-AMCase (207169; Abcam) followed by goat anti-rabbit IgG (H + L)–HRP (4049-05; SouthernBiotech) (table S1). Total BAL protein quantities were expressed as relative units minus AMCase signal, unless specified otherwise. IL-13 (88-7137-22; Thermo Fisher Scientific), IL-33 (DY362605; R&D), and IL-5 (431204; BioLegend) were quantified by enzyme-linked immunosorbent assay. Hydroxyproline was determined as previously described (9), by homogenizing snap-frozen whole lung tissue before hydrolysis in concentrated hydrochloric acid for 3 hours at 120°C, followed by drying and incubation with 4-(dimethylamino) benzaldehyde as recommended by the manufacturer (Sigma-Aldrich). Absorbance was measured at 560 nm using a Synergy H1 Plate Reader (BioTek).

Histology and immunofluorescence microscopy

Formaldehyde-fixed, paraffin-embedded mouse lung tissues sections (5 μm) were stained with hematoxylin and eosin (H&E) or Masson's trichrome by standard methods. Cryosections (7 μm) were prepared from paraformaldehyde-fixed, OCT (Sakura)–embedded frozen lung tissue from the indicated reporter mice. For immunofluorescence imaging, OCT-embedded lung tissue sections were washed three times in PBS at room temperature for at least 5 min and blocked with blocking solution [1:100 diluted goat serum (Thermo Fisher Scientific, 50197Z) and 2% BSA in PBS] for 2 hours at room temperature, followed by incubation for 24 hours at 4°C with primary antibody as listed in table S1, in blocking solution. After washing three times in PBS, the samples were stained for 1 hour at room temperature with a secondary antibody diluted in blocking solution. The nuclei were stained with DAPI and mounted with Fluoromount-G mounting medium (Thermo Fisher Scientific; 00-4958-02) before acquiring images with an AxioImager Z2 microscope or Axio Scan Z1 slide scanner (Carl Zeiss) at the Washington

University Center for Cellular Imaging. An Orca Flash sCMOS camera (Hamamatsu) with a light-emitting diode illumination source and filter sets for DAPI, GFP, and red fluorescent protein imaging were used to acquire fluorescence images at 20× magnification. A color charge-coupled device camera (Carl Zeiss) was used to acquire H&E images at 20× magnification. Image analysis of H&E and immunofluorescence slides was performed using QuPath software (version 0.2.3) (63). Briefly, tissue was detected by thresholding a downsampled and smoothed image of the core, and individual cells were identified by separating stains using color deconvolution and identifying peaks in each channel (or sum of the hematoxylin channels) after smoothing and assigning these as positive or negative cells (64). The percentage of positive cells per area was calculated, and the results were exported along with markup images showing the detected cells for visual verification.

RNA sequencing

Lung alveolar epithelial type 2 cells (AT2s) (DAPI$^-$CD45$^-$EpCAM$^+$MHCII^{hi}) and AEPs (DAPI$^-$CD45$^-$EpCAM$^+$MHCII^{lo}) were sorted as described above and prepared according to the library kit manufacturer's protocol, indexed, pooled, and sequenced on an Illumina NovoSeq 6000 (Illumina). Gene counts were imported into the R/Bioconductor package EdgeR (65) and normalized for library size after calculating trimmed mean of M values (TMM). Ribosomal genes and genes not expressed at greater than one count per million in a number of samples equal to the smallest group size minus one were excluded, TMM size factors and count matrices were imported into Limma (66), and weighted likelihoods based on mean-variance relationships were calculated with voomWithQualityWeights (67). Differential expression results were filtered for Benjamini-Hochberg false discovery rate–adjusted P values of 0.05 or less. For each contrast identified using Limma, global perturbations in established Gene Ontology (GO) terms and KEGG pathways were identified using the GAGE package from R/Bioconductor (68). This package tested for expression changes in log$_2$-fold changes reported by Limma in each term, compared with the background log$_2$-fold changes of genes not included in that term. Heatmaps for each GO term with a Benjamini-Hochberg false discovery rate–adjusted P value of 0.05 or lower were generated using the R/Bioconductor package heatmap3 (69) to visualize differences across groups of samples.

scRNA-seq was performed as described (70) on WT (DAPI$^-$CD45$^-$EpCAM$^+$) or CR$^+$ (DAPI$^-$CD45$^-$EpCAM$^+$CR$^+$) epithelial cells, sorted into ice-cold 0.5% BSA in PBS, and processed through the Chromium Single-Cell 3′ v2 Library Kit (10X Genomics) per the manufacturer's protocol. Single-cell libraries from 10,000 cells per sample were sequenced with standard Illumina sequencing primers on an Illumina HiSeq 4000, using paired-end sequencing with single indexing, in which read 1 comprised 26 cycles and read 2 comprised 98 cycles. The resulting bcl files were demultiplexed using bcl2fastq2.1.7v, and the resultant paired-end fastq files were aligned to the mm10 transcriptome (71, 72) using STAR aligner in the Cellranger toolkit (10X Genomics). Lung cell plots shown in fig. S1 (A to C) were generated from scRNA-seq data (GEO accession number: GSE149563) (21) accessed via the LungMAP Consortium and Data Coordinating Center (73).

Quantitative RT-PCR

Sorted AEPs (CD45$^-$EpCAM$^+$MHCII^{lo}) were lysed in RLT Plus. Total RNA was then eluted from RNeasy Plus Micro columns

(Qiagen). Total RNA was reverse-transcribed with SuperScript IV VILO, and then quantitative real-time reverse transcription polymerase chain reaction (RT-PCR) using Power SYBR Green (Thermo Fisher Scientific) was run on a CFX Connect Real-Time System (Bio-Rad). Transcripts were normalized to the 18S ribosomal gene, and relative gene expression was determined via the comparative ΔCT ($2^{-\Delta\Delta CT}$) method. Primer pair sequences (listed 5′ to 3′): *Chia1*: (F) TACCAGACAGGCTGGGTTCT; (R) GGAGTAGTCACTGGCTCGGA. 18S: (F) TTACAGGGCCTCGAAAAGAGTC; (R) AACTTTGGCATTGTGGAAGG.

Statistical analysis

Data represent means $\pm$ SE, and results from independent experiments were pooled unless otherwise indicated. *P* values were calculated via unpaired two-tailed Student's *t* test, multiple *t* test, or one-way or two-way analysis of variance (ANOVA) as indicated using Prism software (GraphPad).

Supplementary Materials

The PDF file includes:
Figs. S1 to S13
Table S1

Other Supplementary Material for this manuscript includes the following:
Data files S1 and S2
MDAR Reproducibility Checklist

REFERENCES AND NOTES

1. Q. Di, Y. Wang, A. Zanobetti, Y. Wang, P. Koutrakis, C. Choirat, F. Dominici, J. D. Schwartz, Air pollution and mortality in the Medicare population. *N. Engl. J. Med.* **376**, 2513–2522 (2017).

2. A. J. Cohen, M. Brauer, R. Burnett, H. R. Anderson, J. Frostad, K. Estep, K. Balakrishnan, B. Brunekreef, L. Dandona, R. Dandona, V. Feigin, G. Freedman, B. Hubbell, A. Jobling, H. Kan, L. Knibbs, Y. Liu, R. Martin, L. Morawska, C. A. Pope III, H. Shin, K. Straif, G. Shaddick, M. Thomas, R. van Dingenen, A. van Donkelaar, T. Vos, C. J. L. Murray, M. H. Forouzanfar, Estimates and 25-year trends of the global burden of disease attributable to ambient air pollution: An analysis of data from the Global Burden of Diseases Study 2015. *Lancet* **389**, 1907–1918 (2017).

3. B. D. Horne, E. A. Joy, M. G. Hofmann, P. H. Gesteland, J. B. Cannon, J. S. Lefler, D. P. Blagev, E. K. Korgenski, N. Torosyan, G. I. Hansen, D. Kartchner, C. A. Pope III, Short-term elevation of fine particulate matter air pollution and acute lower respiratory infection. *Am. J. Respir. Crit. Care Med.* **198**, 759–766 (2018).

4. M. C. Basil, J. Katzen, A. E. Engler, M. Guo, M. J. Herriges, J. J. Kathiriya, R. Windmueller, A. B. Ysasi, W. J. Zacharias, H. A. Chapman, D. N. Kotton, J. R. Rock, H.-W. Snoeck, G. Vunjak-Novakovic, J. A. Whitsett, E. E. Morrisey, The cellular and physiological basis for lung repair and regeneration: Past, present, and future. *Cell Stem Cell* **26**, 482–502 (2020).

5. Y. Yao, J. Pan, Z. Liu, X. Meng, W. Wang, H. Kan, W. Wang, Temporal association between particulate matter pollution and case fatality rate of COVID-19 in Wuhan. *Environ. Res.* **189**, 109941 (2020).

6. L. A. Stevenson, P. J. Gergen, D. R. Hoover, D. Rosenstreich, D. M. Mannino, T. D. Matte, Sociodemographic correlates of indoor allergen sensitivity among United States children. *J. Allergy Clin. Immunol.* **108**, 747–752 (2001).

7. S. J. Van Dyken, D. Garcia, P. Porter, X. Huang, P. J. Quinlan, P. D. Blanc, D. B. Corry, R. M. Locksley, Fungal chitin from asthma-associated home environments induces eosinophilic lung infiltration. *J. Immunol.* **187**, 2261–2267 (2011).

8. P. M. Salo, S. J. Arbes Jr., R. Jaramillo, A. Calatroni, C. H. Weir, M. L. Sever, J. A. Hoppin, K. M. Rose, A. H. Liu, P. J. Gergen, H. E. Mitchell, D. C. Zeldin, Prevalence of allergic sensitization in the United States: Results from the National Health and Nutrition Examination Survey (NHANES) 2005-2006. *J. Allergy Clin. Immunol.* **134**, 350–359 (2014).

9. S. J. Van Dyken, H.-E. Liang, R. P. Naikawadi, P. G. Woodruff, P. J. Wolters, D. J. Erle, R. M. Locksley, Spontaneous chitin accumulation in airways and age-related fibrotic lung disease. *Cell* **169**, 497–509.e13 (2017).

10. K. Yasuda, T. Muto, T. Kawagoe, M. Matsumoto, Y. Sasaki, K. Matsushita, Y. Taki, S. Futatsugi-Yumikura, H. Tsutsui, K. J. Ishii, T. Yoshimoto, S. Akira, K. Nakanishi, Contribution of IL-33-activated type II innate lymphoid cells to pulmonary eosinophilia in intestinal nematode-infected mice. *Proc. Natl. Acad. Sci. U.S.A.* **109**, 3451–3456 (2012).

11. S. J. Van Dyken, A. Mohapatra, J. C. Nussbaum, A. B. Molofsky, E. E. Thornton, S. F. Ziegler, A. N. J. McKenzie, M. F. Krummel, H.-E. Liang, R. M. Locksley, Chitin activates parallel immune modules that direct distinct inflammatory responses via innate lymphoid type 2 and γδ T cells. *Immunity* **40**, 414–424 (2014).

12. A. Mohapatra, S. J. Van Dyken, C. Schneider, J. C. Nussbaum, H.-E. Liang, R. M. Locksley, Group 2 innate lymphoid cells utilize the IRF4-IL-9 module to coordinate epithelial cell maintenance of lung homeostasis. *Mucosal Immunol.* **9**, 275–286 (2016).

13. D.-H. Kim, Y. Wang, H. Jung, R. L. Field, X. Zhang, T.-C. Liu, C. Ma, J. S. Fraser, J. R. Brestoff, S. J. Van Dyken, A type 2 immune circuit in the stomach controls mammalian adaptation to dietary chitin. *Science* **381**, 1092–1098 (2023).

14. C. Lucas, P. Wong, J. Klein, T. B. R. Castro, J. Silva, M. Sundaram, M. K. Ellingson, T. Mao, J. E. Oh, B. Israelow, T. Takahashi, M. Tokuyama, P. Lu, A. Venkataraman, A. Park, S. Mohanty, H. Wang, A. L. Wyllie, C. B. F. Vogels, R. Earnest, S. Lapidus, I. M. Ott, A. J. Moore, M. C. Muenker, J. B. Fournier, M. Campbell, C. D. Odio, A. Casanovas-Massana, Yale IMPACT Team, R. Herbst, A. C. Shaw, R. Medzhitov, W. L. Schulz, N. D. Grubaugh, C. Dela Cruz, S. Farhadian, A. I. Ko, S. B. Omer, A. Iwasaki, Longitudinal analyses reveal immunological misfiring in severe COVID-19. *Nature* **584**, 463–469 (2020).

15. C. Page, L. Goicochea, K. Matthews, Y. Zhang, P. Klover, M. J. Holtzman, L. Hennighausen, M. Frieman, Induction of alternatively activated macrophages enhances pathogenesis during severe acute respiratory syndrome coronavirus infection. *J. Virol.* **86**, 13334–13349 (2012).

16. C. Huang, Y. Wang, X. Li, L. Ren, J. Zhao, Y. Hu, L. Zhang, G. Fan, J. Xu, X. Gu, Z. Cheng, T. Yu, J. Xia, Y. Wei, W. Wu, X. Xie, W. Yin, H. Li, M. Liu, Y. Xiao, H. Gao, L. Guo, J. Xie, G. Wang, R. Jiang, Z. Gao, Q. Jin, J. Wang, B. Cao, Clinical features of patients infected with 2019 novel coronavirus in Wuhan, China. *Lancet* **395**, 497–506 (2020).

17. T. A. Reese, H.-E. Liang, A. M. Tager, A. D. Luster, N. Van Rooijen, D. Voehringer, R. M. Locksley, Chitin induces accumulation in tissue of innate immune cells associated with allergy. *Nature* **447**, 92–96 (2007).

18. B. Treutlein, D. G. Brownfield, A. R. Wu, N. F. Neff, G. L. Mantalas, F. H. Espinoza, T. J. Desai, M. A. Krasnow, S. R. Quake, Reconstructing lineage hierarchies of the distal lung epithelium using single-cell RNA-seq. *Nature* **509**, 371–375 (2014).

19. A. Jacob, M. Morley, F. Hawkins, K. B. McCauley, J. C. Jean, H. Heins, C.-L. Na, T. E. Weaver, M. Vedaie, K. Hurley, A. Hinds, S. J. Russo, S. Kook, W. Zacharias, M. Ochs, K. Traber, L. J. Quinton, A. Crane, B. R. Davis, F. V. White, J. Wambach, J. A. Whitsett, F. S. Cole, E. E. Morrisey, S. H. Guttentag, M. F. Beers, D. N. Kotton, Differentiation of human pluripotent stem cells into functional lung alveolar epithelial cells. *Cell Stem Cell* **21**, 472–488.e10 (2017).

20. X. Han, R. Wang, Y. Zhou, L. Fei, H. Sun, S. Lai, A. Saadatpour, Z. Zhou, H. Chen, F. Ye, D. Huang, Y. Xu, W. Huang, M. Jiang, X. Jiang, J. Mao, Y. Chen, C. Lu, J. Xie, Q. Fang, Y. Wang, R. Yue, T. Li, H. Huang, S. H. Orkin, G.-C. Yuan, M. Chen, G. Guo, Mapping the mouse cell atlas by Microwell-Seq. *Cell* **172**, 1091–1107.e17 (2018).

21. J. A. Zepp, M. P. Morley, C. Loebel, M. M. Kremp, F. N. Chaudhry, M. C. Basil, J. P. Leach, D. C. Liberti, T. K. Niethamer, Y. Ying, S. Jayachandran, A. Babu, S. Zhou, D. B. Frank, J. A. Burdick, E. E. Morrisey, Genomic, epigenomic, and biophysical cues controlling the emergence of the lung alveolus. *Science* **371**, eabc3172 (2021).

22. M. Corti, A. R. Brody, J. H. Harrison, Isolation and primary culture of murine alveolar type II cells. *Am. J. Respir. Cell Mol. Biol.* **14**, 309–315 (1996).

23. H. A. Chapman, X. Li, J. P. Alexander, A. Brumwell, W. Lorizio, K. Tan, A. Sonnenberg, Y. Wei, T. H. Vu, Integrin αβ4 identifies an adult distal lung epithelial population with regenerative potential in mice. *J. Clin. Invest.* **121**, 2855–2862 (2011).

24. W. J. Zacharias, D. B. Frank, J. A. Zepp, M. P. Morley, F. A. Alkhaleel, J. Kong, S. Zhou, E. Cantu, E. E. Morrisey, Regeneration of the lung alveolus by an evolutionarily conserved epithelial progenitor. *Nature* **555**, 251–255 (2018).

25. M. Strunz, L. M. Simon, M. Ansari, J. J. Kathiriya, I. Angelidis, C. H. Mayr, G. Tsidiridis, M. Lange, L. F. Mattner, M. Yee, P. Ogar, A. Sengupta, I. Kukhtevich, R. Schneider, Z. Zhao, C. Voss, T. Stoeger, J. H. L. Neumann, A. Hilgendorff, J. Behr, M. O'Reilly, M. Lehmann, G. Burgstaller, M. Königshoff, H. A. Chapman, F. J. Theis, H. B. Schiller, Alveolar regeneration through a Krt8+ transitional stem cell state that persists in human lung fibrosis. *Nat. Commun.* **11**, 3559 (2020).

26. Y. Kobayashi, A. Tata, A. Konkimalla, H. Katsura, R. F. Lee, J. Ou, N. E. Banovich, J. A. Kropski, P. R. Tata, Persistence of a regeneration-associated, transitional alveolar epithelial cell state in pulmonary fibrosis. *Nat. Cell Biol.* **22**, 934–946 (2020).

27. J. Choi, J.-E. Park, G. Tsagkogeorga, M. Yanagita, B.-K. Koo, N. Han, J.-H. Lee, Inflammatory signals induce AT2 cell-derived damage-associated transient progenitors that mediate alveolar regeneration. *Cell Stem Cell* **27**, 366–382.e7 (2020).

28. T. M. Delorey, C. G. K. Ziegler, G. Heimberg, R. Normand, Y. Yang, Å. Segerstolpe, D. Abbondanza, S. J. Fleming, A. Subramanian, D. T. Montoro, K. A. Jagadeesh, K. K. Dey, P. Sen, M. Slyper, Y. H. Pita-Juárez, D. Phillips, J. Biermann, Z. Bloom-Ackermann, N. Barkas, A. Ganna, J. Gomez, J. C. Melms, I. Katsyv, E. Normandin, P. Naderi, Y. V. Popov, S. S. Raju, S. Niezen, L. T.-Y. Tsai, K. J. Siddle, M. Sud, V. M. Tran, S. K. Vellarikkal, Y. Wang, L. Amir-Zilberstein, D. S. Atri, J. Beechem, O. R. Brook, J. Chen, P. Divakar, P. Dorceus, J. M. Engreitz, A. Essene, D. M. Fitzgerald, R. Fropf, S. Gazal, J. Gould, J. Grzyb, T. Harvey,

J. Hecht, T. Hether, J. Jané-Valbuena, M. Leney-Greene, H. Ma, C. McCabe, D. E. McLoughlin, E. M. Miller, C. Muus, M. Niemi, R. Padera, L. Pan, D. Pant, C. Pe'er, J. Pfiffner-Borges, C. J. Pinto, J. Plaisted, J. Reeves, M. Ross, M. Rudy, E. H. Rueckert, M. Siciliano, A. Sturm, E. Todres, A. Waghray, S. Warren, S. Zhang, D. R. Zollinger, L. Cosimi, R. M. Gupta, N. Hacohen, H. Hibshoosh, W. Hide, A. L. Price, J. Rajagopal, P. R. Tata, S. Riedel, G. Szabo, T. L. Tickle, P. T. Ellinor, D. Hung, P. C. Sabeti, R. Novak, R. Rogers, D. E. Ingber, Z. G. Jiang, D. Juric, M. Babadi, S. L. Farhi, B. Izar, J. R. Stone, I. S. Vlachos, I. H. Solomon, O. Ashenberg, C. B. M. Porter, B. Li, A. K. Shalek, A.-C. Villani, O. Rozenblatt-Rosen, A. Regev, COVID-19 tissue atlases reveal SARS-CoV-2 pathology and cellular targets. *Nature* **595**, 107–113 (2021).

29. J. C. Melms, J. Biermann, H. Huang, Y. Wang, A. Nair, S. Tagore, I. Katsyv, A. F. Rendeiro, A. D. Amin, D. Schapiro, C. J. Frangieh, A. M. Luoma, A. Filliol, Y. Fang, H. Ravichandran, M. G. Clausi, G. A. Alba, M. Rogava, S. W. Chen, P. Ho, D. T. Montoro, A. E. Kornberg, A. S. Han, M. F. Bakhoum, N. Anandasabapathy, M. Suárez-Fariñas, S. F. Bakhoum, Y. Bram, A. Borczuk, X. V. Guo, J. H. Lefkowitch, C. Marboe, S. M. Lagana, A. Del Portillo, E. J. Tsai, E. Zorn, G. S. Markowitz, R. F. Schwabe, R. E. Schwartz, O. Elemento, A. Saqi, H. Hibshoosh, J. Que, B. Izar, A molecular single-cell lung atlas of lethal COVID-19. *Nature* **595**, 114–119 (2021).

30. K. H. Dinnon III, S. R. Leist, K. Okuda, H. Dang, E. J. Fritch, K. L. Gully, G. De la Cruz, M. D. Evangelista, T. Asakura, R. C. Gilmore, P. Hawkins, S. Nakano, A. West, A. Schäfer, L. E. Gralinski, J. L. Everman, S. P. Sajuthi, M. R. Zweigart, S. Dong, J. McBride, M. R. Cooley, J. B. Hines, M. K. Love, S. D. Groshong, A. VanSchoiack, S. J. Phelan, Y. Liang, T. Hether, M. Leon, R. E. Zumwalt, L. M. Barton, E. J. Duval, S. Mukhopadhyay, E. Stroberg, A. Borczuk, L. B. Thorne, M. K. Sakthivel, Y. Z. Lee, J. S. Hagood, J. R. Mock, M. A. Seibold, W. K. O'Neal, S. A. Montgomery, R. C. Boucher, R. S. Baric, SARS-CoV-2 infection produces chronic pulmonary epithelial and immune cell dysfunction with fibrosis in mice. *Sci. Transl. Med.* **14**, eabo5070 (2022).

31. J. D. Planer, E. E. Morrisey, After the storm: Regeneration, repair, and reestablishment of homeostasis between the alveolar epithelium and innate immune system following viral lung injury. *Annu. Rev. Pathol.* **18**, 337–359 (2023).

32. Y. Jia, K. Chen, P. Lin, G. Lieber, M. Nishi, R. Yan, Z. Wang, Y. Yao, Y. Li, B. A. Whitson, P. Duann, H. Li, X. Zhou, H. Zhu, H. Takeshima, J. C. Hunter, R. L. McLeod, N. Weisleder, C. Zeng, J. Ma, Treatment of acute lung injury by targeting MG53-mediated cell membrane repair. *Nat. Commun.* **5**, 4387 (2014).

33. Y. Mikami, R. Grubb, T. D. Rogers, H. Dang, T. Asakura, P. Kota, R. C. Gilmore, K. Okuda, L. C. Morton, L. Sun, G. Chen, J. A. Wykoff, C. Ehre, J. Vilar, C. van Heusden, A. Livraghi-Butrico, M. Gentzsch, B. Button, M. J. Stutts, S. H. Randell, W. K. O'Neal, R. C. Boucher, Chronic airway epithelial hypoxia exacerbates injury in muco-obstructive lung disease through mucus hyperconcentration. *Sci. Transl. Med.* **15**, eabo7728 (2023).

34. H. E. Ghoneim, P. G. Thomas, J. A. McCullers, Depletion of alveolar macrophages during influenza infection facilitates bacterial superinfections. *J. Immunol.* **191**, 1250–1259 (2013).

35. C. Schneider, S. P. Nobs, A. K. Heer, M. Kurrer, G. Klinke, N. van Rooijen, J. Vogel, M. Kopf, Alveolar macrophages are essential for protection from respiratory failure and associated morbidity following influenza virus infection. *PLOS Pathog.* **10**, e1004053 (2014).

36. L. A. Monticelli, G. F. Sonnenberg, M. C. Abt, T. Alenghat, C. G. K. Ziegler, T. A. Doering, J. M. Angelosanto, B. J. Laidlaw, C. Y. Yang, T. Sathaliyawala, M. Kubota, D. Turner, J. M. Diamond, A. W. Goldrath, D. L. Farber, R. G. Collman, E. J. Wherry, D. Artis, Innate lymphoid cells promote lung-tissue homeostasis after infection with influenza virus. *Nat. Immunol.* **12**, 1045–1054 (2011).

37. D. Califano, Y. Furuya, S. Roberts, D. Avram, A. N. J. McKenzie, D. W. Metzger, IFN-γ increases susceptibility to influenza A infection through suppression of group II innate lymphoid cells. *Mucosal Immunol.* **11**, 209–219 (2018).

38. S. J. Van Dyken, J. C. Nussbaum, J. Lee, A. B. Molofsky, H.-E. Liang, J. L. Pollack, R. E. Gate, G. E. Haliburton, C. J. Ye, A. Marson, D. J. Erle, R. M. Locksley, A tissue checkpoint regulates type 2 immunity. *Nat. Immunol.* **17**, 1381–1387 (2016).

39. A. O. Hassan, J. B. Case, E. S. Winkler, L. B. Thackray, N. M. Kafai, A. L. Bailey, B. T. McCune, J. M. Fox, R. E. Chen, W. B. Alsoussi, J. S. Turner, A. J. Schmitz, T. Lei, S. Shrihari, S. P. Keeler, D. H. Fremont, S. Greco, P. B. McCray Jr., S. Perlman, M. J. Holtzman, A. H. Ellebedy, M. S. Diamond, A SARS-CoV-2 infection model in mice demonstrates protection by neutralizing antibodies. *Cell* **182**, 744–753.e4 (2020).

40. T. H. Sisson, M. Mendez, K. Choi, N. Subbotina, A. Courey, A. Cunningham, A. Dave, J. F. Engelhardt, X. Liu, E. S. White, V. J. Thannickal, B. B. Moore, P. J. Christensen, R. H. Simon, Targeted injury of type II alveolar epithelial cells induces pulmonary fibrosis. *Am. J. Respir. Crit. Care Med.* **181**, 254–263 (2010).

41. C. Yao, X. Guan, G. Carraro, T. Parimon, X. Liu, G. Huang, A. Mulay, H. J. Soukiasian, G. David, S. S. Weigt, J. A. Belperio, P. Chen, D. Jiang, P. W. Noble, B. R. Stripp, Senescence of alveolar type 2 cells drives progressive pulmonary fibrosis. *Am. J. Respir. Crit. Care Med.* **203**, 707–717 (2021).

42. R. M. Roy, M. Wüthrich, B. S. Klein, Chitin elicits CCL2 from airway epithelial cells and induces CCR2-dependent innate allergic inflammation in the lung. *J. Immunol.* **189**, 2545–2552 (2012).

43. L. A. Monticelli, L. C. Osborne, M. Noti, S. V. Tran, D. M. W. Zaiss, D. Artis, IL-33 promotes an innate immune pathway of intestinal tissue protection dependent on amphiregulin-EGFR interactions. *Proc. Natl. Acad. Sci. U.S.A.* **112**, 10762–10767 (2015).

44. J. S. Kim, V. S. McKinnis, A. Nawrocki, S. R. White, Stimulation of migration and wound repair of guinea-pig airway epithelial cells in response to epidermal growth factor. *Am. J. Respir. Cell Mol. Biol.* **18**, 66–74 (1998).

45. F. Kheradmand, H. G. Folkesson, L. Shum, R. Derynk, R. Pytela, M. A. Matthay, Transforming growth factor-alpha enhances alveolar epithelial cell repair in a new in vitro model. *Am. J. Physiol.* **267**, L728–L738 (1994).

46. M. Nava, P. Dutta, N. R. Zemke, R. Farias-Eisner, J. V. Vadgama, Y. Wu, Transcriptomic and ChIP-sequence interrogation of EGFR signaling in HER2+ breast cancer cells reveals a dynamic chromatin landscape and S100 genes as targets. *BMC Med. Genomics* **12**, 32 (2019).

47. A. M. Tsou, H. Yano, C. N. Parkhurst, T. Mahlakõiv, C. Chu, W. Zhang, Z. He, K. J. Jarick, C. Zhong, G. G. Putzel, M. Hatazaki, JRI IBD Live Cell Bank Consortium, I. C. Lorenz, D. Andrew, P. Balderes, C. S. N. Klose, S. A. Lira, D. Artis, Neuropeptide regulation of non-redundant ILC2 responses at barrier surfaces. *Nature* **611**, 787–793 (2022).

48. R. R. Ricardo-Gonzalez, M. E. Kotas, C. E. O'Leary, K. Singh, W. Damsky, C. Liao, E. Arouge, I. Tenvooren, D. M. Marquez, A. W. Schroeder, J. N. Cohen, M. S. Fassett, J. Lee, S. G. Daniel, K. Bittinger, R. E. Díaz, J. S. Fraser, N. Ali, K. M. Ansel, M. H. Spitzer, H.-E. Liang, R. M. Locksley, Innate type 2 immunity controls hair follicle commensalism by *Demodex* mites. *Immunity* **55**, 1891–1908.e12 (2022).

49. L. A. Pittet, L. Hall-Stoodley, M. R. Rutkowski, A. G. Harmsen, Influenza virus infection decreases tracheal mucociliary velocity and clearance of Streptococcus pneumoniae. *Am. J. Respir. Cell Mol. Biol.* **42**, 450–460 (2010).

50. B. B. Ural, D. P. Caron, P. Dogra, S. B. Wells, P. A. Szabo, T. Granot, T. Senda, M. M. L. Poon, N. Lam, P. Thapa, Y. S. Lee, M. Kubota, R. Matsumoto, D. L. Farber, Inhaled particulate accumulation with age impairs immune function and architecture in human lung lymph nodes. *Nat. Med.* **28**, 2622–2632 (2022).

51. R. L. Chua, S. Lukassen, S. Trump, B. P. Hennig, D. Wendisch, F. Pott, O. Debnath, L. Thürmann, F. Kurth, M. T. Völker, J. Kazmierski, B. Timmermann, S. Twardziok, S. Schneider, F. Machleidt, H. Müller-Redetzky, M. Maier, A. Krannich, S. Schmidt, F. Balzer, J. Liebig, J. Loske, N. Suttorp, J. Eils, N. Ishaque, U. G. Liebert, C. von Kalle, A. Hocke, M. Witzenrath, C. Goffinet, C. Drosten, S. Laudi, I. Lehmann, C. Conrad, L.-E. Sander, R. Eils, COVID-19 severity correlates with airway epithelium-immune cell interactions identified by single-cell analysis. *Nat. Biotechnol.* **38**, 970–979 (2020).

52. J. Ordovas-Montanes, D. F. Dwyer, S. K. Nyquist, K. M. Buchheit, M. Vukovic, C. Deb, M. H. Wadsworth II, T. K. Hughes, S. W. Kazer, T. Yoshimoto, K. N. Cahill, N. Bhattacharyya, H. R. Katz, B. Berger, T. M. Laidlaw, J. A. Boyce, N. A. Barrett, A. K. Shalek, Allergic inflammatory memory in human respiratory epithelial progenitor cells. *Nature* **560**, 649–654 (2018).

53. R. R. Ricardo-Gonzalez, M. E. Kotas, I. Tenvooren, D. M. Marquez, M. S. Fassett, J. Lee, S. G. Daniel, K. Bittinger, R. E. Díaz, J. S. Fraser, K. Mark Ansel, M. H. Spitzer, H.-E. Liang, R. M. Locksley, Type 2 innate immunity regulates hair follicle homeostasis to control Demodex pathosymbionts. bioRxiv 437438 [Preprint] (2021); https://doi.org/10.1101/2021.03.29.437438.

54. M. A. Seibold, T. A. Reese, S. Choudhry, M. T. Salam, K. Beckman, C. Eng, A. Atakilit, K. Meade, M. Lenoir, H. G. Watson, S. Thyne, R. Kumar, K. B. Weiss, L. C. Grammer, P. Avila, R. P. Schleimer, J. V. Fahy, J. Rodriguez-Santana, W. Rodriguez-Cintron, R. G. Boot, D. Sheppard, F. D. Gilliland, R. M. Locksley, E. G. Burchard, Differential enzymatic activity of common haplotypic versions of the human acidic mammalian chitinase protein. *J. Biol. Chem.* **284**, 19650–19658 (2009).

55. K. Okawa, M. Ohno, A. Kashimura, M. Kimura, Y. Kobayashi, M. Sakaguchi, Y. Sugahara, M. Kamaya, Y. Kino, P. O. Bauer, F. Oyama, Loss and gain of human acidic mammalian chitinase activity by nonsynonymous SNPs. *Mol. Biol. Evol.* **33**, 3183–3193 (2016).

56. T. E. Sutherland, O. A. Andersen, M. Betou, I. M. Eggleston, R. M. Maizels, D. van Aalten, J. E. Allen, Analyzing airway inflammation with chemical biology: Dissection of acidic mammalian chitinase function with a selective drug-like inhibitor. *Chem. Biol.* **18**, 569–579 (2011).

57. M. Kimura, T. Umeyama, S. Wakita, K. Okawa, M. Sakaguchi, V. Matoska, P. O. Bauer, F. Oyama, Direct comparison of chitinolytic properties and determination of combinatory effects of mouse chitotriosidase and acidic mammalian chitinase. *Int. J. Biol. Macromol.* **134**, 882–890 (2019).

58. B. A. Barad, L. Liu, R. E. Diaz, R. Basilio, S. J. Van Dyken, R. M. Locksley, J. S. Fraser, Differences in the chitinolytic activity of mammalian chitinases on soluble and insoluble substrates. *Protein Sci.* **29**, 966–977 (2020).

59. H.-E. Liang, R. L. Reinhardt, J. K. Bando, B. M. Sullivan, I.-C. Ho, R. M. Locksley, Divergent expression patterns of IL-4 and IL-13 define unique functions in allergic immunity. *Nat. Immunol.* **13**, 58–66 (2011).

60. D. R. Herbert, C. Hölscher, M. Mohrs, B. Arendse, A. Schwegmann, M. Radwanska, M. Leeto, R. Kirsch, P. Hall, H. Mossmann, B. Claussen, I. Förster, F. Brombacher, Alternative macrophage activation is essential for survival during schistosomiasis and downmodulates T helper 1 responses and immunopathology. *Immunity* **20**, 623–635 (2004).

61. Z. Chong, C. E. Karl, P. J. Halfmann, Y. Kawaoka, E. S. Winkler, S. P. Keeler, M. J. Holtzman, J. Yu, M. S. Diamond, Nasally delivered interferon-λ protects mice against infection by SARS-CoV-2 variants including Omicron. *Cell Rep.* **39**, 110799 (2022).

62. R. E. Díaz, A. K. Ecker, G. J. Correy, P. Asthana, I. D. Young, B. Faust, M. C. Thompson, I. B. Seiple, S. Van Dyken, R. M. Locksley, J. S. Fraser, Structural characterization of ligand binding and pH-specific enzymatic activity of mouse acidic mammalian chitinase. *eLife* **12**, RP89918 (2024).

63. Qupath software; https://qupath.github.io/.

64. P. Bankhead, M. B. Loughrey, J. A. Fernández, Y. Dombrowski, D. G. McArt, P. D. Dunne, S. McQuaid, R. T. Gray, L. J. Murray, H. G. Coleman, J. A. James, M. Salto-Tellez, P. W. Hamilton, QuPath: Open source software for digital pathology image analysis. *Sci. Rep.* **7**, 16878 (2017).

65. M. D. Robinson, D. J. McCarthy, G. K. Smyth, edgeR: A bioconductor package for differential expression analysis of digital gene expression data. *Bioinformatics* **26**, 139–140 (2010).

66. M. E. Ritchie, B. Phipson, D. Wu, Y. Hu, C. W. Law, W. Shi, G. K. Smyth, limma powers differential expression analyses for RNA-sequencing and microarray studies. *Nucleic Acids Res.* **43**, e47 (2015).

67. R. Liu, A. Z. Holik, S. Su, N. Jansz, K. Chen, H. S. Leong, M. E. Blewitt, M.-L. Asselin-Labat, G. K. Smyth, M. E. Ritchie, Why weight? Modelling sample and observational level variability improves power in RNA-seq analyses. *Nucleic Acids Res.* **43**, e97 (2015).

68. W. Luo, M. S. Friedman, K. Shedden, K. D. Hankenson, P. J. Woolf, GAGE: Generally applicable gene set enrichment for pathway analysis. *BMC Bioinformatics* **10**, 161 (2009).

69. S. Zhao, Y. Guo, Q. Sheng, Y. Shyr, Advanced heat map and clustering analysis using heatmap3. *Biomed. Res. Int.* **2014**, 986048 (2014).

70. R. R. Ricardo-Gonzalez, S. J. Van Dyken, C. Schneider, J. Lee, J. C. Nussbaum, H.-E. Liang, D. Vaka, W. L. Eckalbar, A. B. Molofsky, D. J. Erle, R. M. Locksley, Tissue signals imprint ILC2 identity with anticipatory function. *Nat. Immunol.* **19**, 1093–1099 (2018).

71. mm10 transcriptome_1; ftp://ftp.ensembl.org/pub/release-84/fasta/mus_musculus/dna/Mus_musculus.GRCm38.dna.primary_assembly.fa.gz.

72. mm10 transcriptome_2; ftp://ftp.ensembl.org/pub/release-84/gtf/mus_musculus/Mus_musculus.GRCm38.84.gtf.gz.

73. LungMAP Consortium; www.lungmap.net.

74. H. Jung, S. Van Dyken, Lung distal epithelium_ChiaRed and WT epithelial cells (Dryad, 2024).